



# AMERICAN METEOROLOGICAL SOCIETY

*Bulletin of the American Meteorological Society*

## **EARLY ONLINE RELEASE**

This is a preliminary PDF of the author-produced manuscript that has been peer-reviewed and accepted for publication. Since it is being posted so soon after acceptance, it has not yet been copyedited, formatted, or processed by AMS Publications. This preliminary version of the manuscript may be downloaded, distributed, and cited, but please be aware that there will be visual differences and possibly some content differences between this version and the final published version.

The DOI for this manuscript is doi: 10.1175/BAMS-D-16-0244.1

The final published version of this manuscript will replace the preliminary version at the above DOI once it is available.

If you would like to cite this EOR in a separate work, please use the following full citation:

Kustas, W., M. Anderson, J. Alfieri, K. Knipper, A. Torres-Rua, C. Parry, H. Hieto, N. Agam, A. White, F. Gao, L. McKee, J. Prueger, L. Hipps, S. Los, M. Alsina, L. Sanchez, B. Sams, N. Dokoozlian, M. McKee, S. Jones, Y. Yang, T. Wilson, F. Lei, A. McElrone, J. Heitman, A. Howard, K. Post, F. Melton, and C. Hain, 2018: The Grape Remote sensing Atmospheric Profile and Evapotranspiration eXperiment (GRAPEX). Bull. Amer. Meteor. Soc. doi:10.1175/BAMS-D-16-0244.1, in press.



# The Grape Remote sensing Atmospheric Profile and Evapotranspiration eXperiment (GRAPEX)

William P. Kustas<sup>1</sup>, Martha C. Anderson<sup>1</sup>, Joseph G. Alfieri<sup>1</sup>, Kyle Knipper<sup>1</sup>, Alfonso Torres-Rua<sup>2</sup>, Christopher K. Parry<sup>3</sup>, Hector Hieto<sup>4</sup>, Nurit Agam<sup>5</sup>, Alex White<sup>1</sup>, Feng Gao<sup>1</sup>, Lynn McKee<sup>1</sup>, John H. Prueger<sup>6</sup>, Lawrence E. Hipps<sup>7</sup>, Sebastian Los<sup>7</sup>, Maria Alsina<sup>8</sup>, Luis Sanchez<sup>8</sup>, Brent Sams<sup>8</sup>, Nick Dokoozlian<sup>8</sup>, Mac McKee<sup>2</sup>, Scott Jones<sup>7</sup>, Yun Yang<sup>1</sup>, Tiffany G. Wilson<sup>1</sup>, Fangni Lei<sup>1</sup>, Andrew McElrone<sup>3</sup>, Josh L. Heitman<sup>9</sup>, Adam M. Howard<sup>9</sup>, Kirk Post<sup>10</sup>, Forrest Melton<sup>10,11</sup>, Christopher Hain<sup>12</sup>

<sup>1</sup>USDA-ARS, Hydrology and Remote Sensing Laboratory, Beltsville, MD  
Bill.Kustas@ars.usda.gov (W.P.K.); [Martha.Anderson@ars.usda.gov](mailto:Martha.Anderson@ars.usda.gov) (M.C.A.) ;  
Joe.Alfieri@ars.usda.gov (J.G.A.) ; [Kyle.Knipper@ars.usda.gov](mailto:Kyle.Knipper@ars.usda.gov) (K.K.) ;  
[Lynn.McKee@ars.usda.gov](mailto:Lynn.McKee@ars.usda.gov) (L.M.) ; [Alex.White@ars.usda.gov](mailto:Alex.White@ars.usda.gov) (A.W.) ;  
[Feng.Gao@ars.usda.gov](mailto:Feng.Gao@ars.usda.gov) (F.G.), [Yun.Yang@ars.usda.gov](mailto:Yun.Yang@ars.usda.gov) (Y.Y.), [Tiffany.Wilson@ars.usda.gov](mailto:Tiffany.Wilson@ars.usda.gov)  
(T.G.W.), [Fangni.Lei@ars.usda.gov](mailto:Fangni.Lei@ars.usda.gov) (F.L.)

<sup>2</sup>Utah Water Research Laboratory, Utah State University, Logan, UT  
[Alfonso.Torres@usu.edu](mailto:Alfonso.Torres@usu.edu) (A.T-R.) ; [Mac.McKee@usu.edu](mailto:Mac.McKee@usu.edu) (M.M.)

<sup>3</sup>USDA-ARS Crops Pathology and Genetics Research, UC Davis, Davis, CA  
[Christopher.Parry@ars.usda.gov](mailto:Christopher.Parry@ars.usda.gov) (C.K.P.) ; [Andrew.McElrone@ars.usda.gov](mailto:Andrew.McElrone@ars.usda.gov) (A.M.)

<sup>4</sup>IRTA-Research & Technology Food & Agriculture, Lleida, Spain  
[Hector.Nieto@irta.cat](mailto:Hector.Nieto@irta.cat)

<sup>5</sup>Jacob Blaustein Institutes for Desert Research, Ben-Gurion University of Negev, Israel  
[Agam@bgu.ac.il](mailto:Agam@bgu.ac.il)

<sup>6</sup>USDA-ARS, National Laboratory for Agriculture and The Environment, Ames, IA  
[John.Prueger@ars.usda.gov](mailto:John.Prueger@ars.usda.gov)

<sup>7</sup>Plants, Soils and Climate Department, Utah State University, Logan UT  
[Lawrence.Hipps@usu.edu](mailto:Lawrence.Hipps@usu.edu) (L.E.H.); [Sebastian.Los@usu.edu](mailto:Sebastian.Los@usu.edu) (S.L.); [Scott.Jones@usu.edu](mailto:Scott.Jones@usu.edu) (S.J.)

<sup>8</sup>E.&J. Gallo Winery, Viticulture, Chemistry and Enology, Modesto, CA  
[MariadelMar.Alsina@ejgallo.com](mailto:MariadelMar.Alsina@ejgallo.com) (M.A.); [Luis.Sanchez@ejgallo.com](mailto:Luis.Sanchez@ejgallo.com) (L.S.);  
[Brent.Sams@ejgallo.com](mailto:Brent.Sams@ejgallo.com) (B.S.); [Nick.Dokoozlian@ejgallo.com](mailto:Nick.Dokoozlian@ejgallo.com) (N.D.)

<sup>9</sup>Soil Science Department, North Carolina State University, Raleigh, NC  
[JLHeitma@ncsu.edu](mailto:JLHeitma@ncsu.edu) (J.L.H.); [AMHoward@ncsu.edu](mailto:AMHoward@ncsu.edu) (A.M.H.)

<sup>10</sup>School of Natural Resources, California State University Monterey Bay, Marina, CA  
[Forrest.S.Melton@nasa.gov](mailto:Forrest.S.Melton@nasa.gov) (F.M.); [KPost@csumb.edu](mailto:KPost@csumb.edu) (K.P.)

<sup>11</sup> NASA Ames Research Center, Moffett Field, CA

<sup>12</sup>NASA-MSFC Huntsville, AL  
[christopher.hain@nasa.gov](mailto:christopher.hain@nasa.gov)

*Corresponding author address:* W.P. Kustas, USDA-ARS, HRSL, 10300 Baltimore Ave,  
Beltsville, MD 20705 Tel: 301-504-8498 Fax: 301-504-8931 Email: [bill.kustas@ars.usda.gov](mailto:bill.kustas@ars.usda.gov)

## **Capsule Summary**

Development of better water management tools is the focus of the GRAPEX (Grape Remote sensing Atmospheric Profile and Evapotranspiration eXperiment) project. An overview of GRAPEX and preliminary results are presented.

## **ABSTRACT**

1 Particularly in light of California's recent multi-year drought, there is a critical need for accurate  
2 and timely evapotranspiration (ET) and crop stress information to ensure long-term sustainability  
3 of high-value crops. Providing this information requires the development of tools applicable  
4 across the continuum from sub-field scales to improve water management within individual  
5 fields up to watershed and regional scales to assess water resources at county and state levels.  
6 High value perennial crops (vineyards and orchards) are major water users and growers will need  
7 better tools to improve water use efficiency to remain economically viable and sustainable  
8 during periods of prolonged drought. In order to develop these tools, government, university, and  
9 industry partners are evaluating a multi-scale remote sensing-based modeling system for  
10 application over vineyards. During the 2013 to 2017 growing seasons, the GRAPEX (Grape  
11 Remote sensing Atmospheric Profile and Evapotranspiration eXperiment) project has collected  
12 micrometeorological and biophysical data within adjacent Pinot noir vineyards in the Central  
13 Valley of California. Additionally, each year ground, airborne and satellite remote sensing data  
14 were collected during Intensive Observation Periods (IOPs) representing different vine  
15 phenological stages. An overview of the measurements and some initial results regarding the  
16 impact of vine canopy architecture on modeling ET and plant stress are presented here.  
17 Refinements to the ET modeling system based on GRAPEX are being implemented initially at  
18 the field scale for validation and then will be integrated into the regional modeling toolkit for  
19 large area assessment.

## INTRODUCTION

As is the case in many parts of the world, agricultural production in California faces the dual challenge of growing demand for limited water resources and increasing interannual variability in rainfall and water availability. As a result, both the state and its agricultural community recognize the need to develop sustainable long-term water management strategies. For example, in response to the recent multi-year drought that has severely depleted both surface and groundwater stores, the California Department of Water Resources enacted the Sustainable Groundwater Management Act (SGMA) in 2014, mandating measures to curtail the severe overdraft of water in regions dependent on groundwater resources. At the same time, many in the agricultural community have taken proactive steps to develop and implement robust water management plans that both reduce consumptive water use and enhance resilience against future droughts and water shortages. As an example, producers of wine grapes – a California crop valued at nearly \$6B annually – have actively sought tools to better monitor crop water status and manage water use.

Currently, the irrigation management decisions for many California crops are based on a combination of in-situ observations of soil moisture, remote sensing-based estimates of Normalized Difference Vegetation Index (NDVI), and the application of the FAO crop model using crop coefficients that have been tuned for specific crops (Allen et al., 1998). Unfortunately, these methods are not sufficiently robust, particularly for highly structured canopies such as vineyards and tree orchards. They cannot accurately separate crop and the combined interrow soil and cover crop water use and the crop coefficients are not easily adjustable for stressed conditions (e.g., Ting et al., 2016). As a result, significant errors in the timing and amount of irrigation relative to crop water needs have led to an over-prescription of irrigation applications. Moreover, later in growing season when deficit irrigation is preferred to conserve water, ensure crop quality, or facilitate harvest, the current approach cannot reliably determine the degree of

crop stress. This has led to the development of thermal-based methods for irrigation scheduling (e.g., Bellvert et al., 2015; 2016)

In 2012, researchers from E&J Gallo Winery approached scientists with the USDA Agricultural Research Service (USDA-ARS) Hydrology and Remote Sensing Laboratory seeking advice on practical methods for using remote sensing from satellites or airborne systems to guide irrigation decisions. Critical decisions in wine grape production include when to begin irrigating in the spring, and timing and amount of water to apply during the growing season that balances vine health with carefully timed periods of mild stress to improve berry quality for wine production. Spatially detailed information regarding vine stress variations across the field is also needed to ensure the judicious application of water only where it is needed. The scientists at E&J Gallo Winery realized that accurate maps of evapotranspiration (ET) at daily to weekly increments and sub-field spatial resolutions could help both reduce water use and enhance crop quality.

This collaboration has evolved into the ongoing GRAPEX (Grape Remote sensing Atmospheric Profile and Evapotranspiration eXperiment) project, and has expanded to include personnel from other USDA-ARS labs, NASA, universities, and industry. The ultimate goal of the project is to provide wine grape producers and, in the longer term, fruit and nut orchard growers with the tools needed to generate high-resolution ET data that can be used to guide water management decisions. These tools will have the advantage over the current “business as usual” approach for assessing water needs by being applicable year-round and by providing water use information with higher spatial and temporal detail. The tools will also differentiate between the water used by the grass cover crop, active early in the growing season, with water uptake by the grapevines themselves. In addition, the project will demonstrate the utility of using very-high resolution imagery collected via Unmanned Aerial Vehicles (UAVs) at critical times

during the growing season to assess in-field variability in vine condition and facilitate precision management.

The Two-Source Energy Balance (TSEB) developed by HRSL scientists and colleagues takes advantage of land-surface temperature (LST) measurements from thermal infrared (TIR) imagery to monitor ET, and has the potential to provide additional information regarding crop stress and soil moisture conditions. The model framework is well-suited to the goals of the GRAPEX project because it partitions evaporative fluxes between the crop canopy and substrate surface (in this case, the soil or cover crop between the vine rows). TSEB can also be run across a range of spatial scales: from sub-field resolutions using airborne data, to larger scales using satellite imagery from both polar orbiting and geostationary platforms. Nonetheless, the unique canopy architecture of vineyards and orchards, which is characterized by strongly clumped vegetation separated by significant interrow spaces containing bare soil or a cover crop, leads to several intriguing modeling and measurement challenges. First, the ET models must be able to partition the bulk moisture flux and crop stress derived from remote sensing-based products (typically at resolutions of 30m or coarser) between the vine canopy and the interrow - environments that will likely have very different thermal characteristics and atmospheric couplings. Also, the structural characteristics of the canopy can significantly influence the turbulent flow and exchange of heat and water vapor from the vineyard; for example, by imposing dependencies on wind direction. Finally, radiation transport through structured canopies can be complex, leading to highly variable shadowing and soil surface fluxes that can confound simple modeling approaches.

To address the effects of these unique characteristics, the standard form of the TSEB model will require modification to optimize its performance over highly-structured crops. Identifying the key factors affecting exchange processes over vineyards will guide the refinements to the remote sensing-based modeling scheme. This project uses in-situ data to investigate the physical

processes controlling turbulent transport and exchange in highly-structured canopies. The GRAPEX project also seeks to use ground-based and UAV data to improve the model parameterization and design for routine application using satellite imagery. One advancement under investigation is the fusion of ET estimates retrieved using satellite data with differing spatial and temporal resolutions to generate “ET datacubes”, *i.e.* a gridded time-series dataset with both high spatial (30 m) and temporal resolutions (daily time steps), which can be used to inform daily water management decisions at field scales.

This paper provides an overview of the measurements collected during GRAPEX along with some preliminary analyses conducted with the data collected to date. We also describe the initial evaluation of the modeling system and discuss plans for future research.

## **SITE AND DATA DESCRIPTION**

### ***Study site and vineyard management***

The data used to refine and evaluate the models were collected in two Pinot noir blocks located within Borden Ranch vineyard near Lodi, CA (38.29 N 121.12 W), in Sacramento County (see Fig. 1), as part of the GRAPEX project. The two adjacent vineyards differ in the age and maturity of the vines, with the north and south vineyards being 6 and 3 years old, respectively, at the beginning the 2013 growing season. The management of the two vineyards – for example, the timing and amount of irrigation, pruning activities, cover crop, and application of agrochemicals – can also differ between blocks and from season to season. Intensive observation Periods (IOPs) described below occurred at different cover crop and vine phenological stages, namely flowering (IOP1), fruit set (IOP2) and veraison (IOP3).

In both fields, the configuration of the trellising system and interrow (Fig. 1) is the same. The vine trellises are 3.35 m apart and run east-west. There is a vine planted every 1.5 m, with the two main vine stems attached to the first cordon at a height of 1.45 m above ground level (agl). There is a second cordon at 1.9 m agl where vine shoots are managed. Typically, the vines reach



a maximum height of between 2.0 m and 2.5 m agl during the growing season with the vine biomass concentrated in the upper half of the total canopy height. The typical vine canopy width is nominally 1 m mid-season. Pruning of the vines is mainly performed to remove shoots growing significantly into the interrow. However, the amount and timing of pruning has varied year-to-year.

Drip irrigation lines run along the base of the trellis at about 30 cm agl with two drip emitters (4 liters/hour) between each vine. In the interrow, the cover crop (a mixture of grasses) is approximately 2 m in width with bare soil on either side (i.e. berm) approximately 0.7 m in width. The cover crop is typically mowed 2-3 times per year and senesces by early June. The berm beneath the vines is kept bare through the use of an herbicide.

### *Continuous measurements*

Beginning with the 2013 growing season, surface fluxes (including ET) and environmental conditions have been measured continuously at both vineyards using eddy covariance micrometeorological systems. These sensor systems are summarized in a schematic and photo of the tower configuration in Figure 2. The tower at each site is instrumented with an infrared gas analyzer (EC150, Campbell Scientific, Logan, Utah, USA<sup>1</sup>) and a sonic anemometer (CSAT3, Campbell Scientific) co-located at 5 m agl to measure the concentrations of water and carbon dioxide and wind velocity, respectively. During the growing season, three additional sonic anemometers mounted at 2.50 m, 3.75 m, and 8 m agl are included on the tower to investigate effects of the canopy structure on near-surface turbulence. Other measurements at the tower include the full radiation budget using a four-component net radiometer (CNR-1, Kipp and Zonen, Delft, Netherlands) mounted at 6 m agl, incident and reflected photosynthetically active radiation (PAR) measured via quantum sensors (LI-190, LI-COR, Lincoln, Nebraska, USA) also

---

<sup>1</sup> The mention of trade names of commercial products in this article is solely for the purpose of providing specific information and does not imply recommendation or endorsement by the US Department of Agriculture.



mounted at 6 m agl, air temperature and water vapor pressure measured using three temperature and humidity probes (HMP45C, Vaisala, Helsinki, Finland) mounted at 2.5 m, 5 m, and 8 m agl, and precipitation measured using a tipping bucket rain gauge (TE-525, Texas Electronics, Dallas, Texas, USA) mounted at 5.5 m agl. Both vine canopy and interrow surface temperatures are measured using a pair of thermal infrared thermometers (SI-111, Campbell Scientific) mounted at 2.5 m agl.

Subsurface measurements include the soil heat flux measured via a cross-row transect of five plates (HFT-3, Radiation Energy Balance Systems, Bellevue, Washington, USA) buried at a depth of 8 cm, soil temperature measured via thermocouples buried at a depth of 2 cm and 6 cm, and soil moisture content measured via a soil moisture probe (SDI-12 HydraProbe, Stevens Water Monitoring Systems, Portland, OR, USA) buried at a depth of 5 cm. In addition, beginning in 2016, a second array of sensors were installed to provide more detailed spatial sampling of soil heat flux (HFT-3, Radiation Energy Balance Systems), water content (HydraProbe, Stevens Water Monitoring Systems) and temperature under the vine canopy and across the interrow. This array consisted of 11 sets of sensors deployed in a hexagonal pattern centered at the mid-row and extended to the vines on either side. An additional profile of temperature, water content, and thermal properties was deployed with the array in order to facilitate the calorimetric approach for determining soil heat flux.

Profiles of soil water content and temperature were also measured under the vines at three locations near each flux tower (Fig. 2) using soil moisture temperature probes (HydraProbe, Stevens Water Monitoring Systems) at depths of 30 cm, 60 cm, and 90 cm. In the north vineyard there were also soil moisture profile measurements at six locations using Decagon (MPS-2 Decagon Pullman Washington, USA) dielectric water potential sensors at depths of approximately 5, 50, 90 and 125 cm, with two Decagon 10HS large soil moisture sensors at 45

cm depth. Additionally, Decagon model G2 and G3 passive capillary lysimeters were installed at two interrow locations (Fig. 2) in the north vineyard for estimating interrow water use.

Sap flow measurements (TDP30, Dynamax Inc., Houston, TX, USA) at 5 locations in both the north and south vineyards (see Figure 2) are collected to estimate the spatial and temporal variability of vine water use and status. The sapflow measurements that lie within the eddy covariance flux footprint are being used together with eddy covariance data in an attempt to separate interrow versus vine plant water use. The passive capillary lysimeter measurements in the interrow will also be helpful in this separation.

In 2015 and 2016 growing seasons, flow meter sensors (manufactured by Mark Battany, University of California Cooperative Extension Viticulture Advisor) for monitoring irrigation (initiation and duration) were used to estimate amount of irrigated water that was applied in both vineyards.

Vine and cover crop development through the growing season as well throughout the whole year were visually tracked using phenocams located across the road on the east side (see Fig. 2) starting in 2013 at the north vineyard and starting in 2015 at the south vineyard. A video of the daily photos collected in the morning (~0900 local time) for the years 2014-2016 for the north vineyard can viewed at <https://www.ars.usda.gov/grapex/phenocam>. Approximately 50 m due west of the flux towers in the north and south vineyard, instrumentation was deployed to measure the surface energy balance following the surface renewal (SR) approach (Paw U et al., 1995). The instruments included a 3D sonic anemometer (81000RE, R.M. Young Company, Traverse city, Michigan, USA), a 76 micrometer diameter Type E thermocouple (FW3, Campbell Scientific, Inc) and a net radiometer (NRLite, Kipp and Zonen), deployed at 2.5 m agl. The SR station design is described in McElrone et al (2013).

## ***Intensive Observation Periods***

### ***Timing of IOPs***

Episodic and intensive data collections, called intensive observation periods (IOPs), were conducted at different vineyard phenological stages during the growing season (see Fig. 1b). In each growing season, the first IOP usually occurred in late April or early May after bud break (grape flowering stage) with low vine cover but significant cover crop biomass. Another IOP often occurred in early to mid-June at the start of the dry season, with rapidly growing vines and fruit (pre-veraison, or berry development stage) and cover crop going through senescence. A third IOP typically occurred in mid to late July or early August, with vines and fruit fully developed (veraison to post veraison stage) and cover crop fully senescent and now acting as a thatch layer. During this period the vines are still actively growing but, through pruning and ripening of the fruit, they are now in a later stage of development. By late August or early September each year, the vineyard grapes reached the required sugar content and were harvested. In 2014, a fourth IOP was conducted in late September after harvest to evaluate vine and interrow cover conditions.

### ***IOP biophysical observations***

During the IOPs, measurements of leaf area index (LAI; LAI-2200 LI-COR, Lincoln, Nebraska, USA), leaf stomatal conductance, photosynthesis and leaf water potential were collected using either a LI-COR (LI6400, LI-COR) or PSP sensor (CIRAS-3, PSP Systems Amesbury, Massachusetts, USA) photosynthesis system and a pressure chamber (615, PMS Instrument Company, Albany, Oregon, USA) along transects across the vineyard (Figure 2) to determine variability in vine biomass, water use and stress. Multispectral measurements in the visible and near-infrared wavelengths, along with leaf-level hyperspectral measurements (FieldSpec 4 Spectroradiometer, ASD Inc., Boulder, Colorado, USA), were also collected so that

satellite and airborne multispectral retrievals could be related to in-situ canopy conditions. Multispectral (4-band) visible and near-infrared measurements using a CROPSCAN (MSR16R, CROPSCAN, Inc., Rochester, Minnesota) instrument mounted on a pole for measuring above the vine canopy were collected over vine and interrow areas as well as a gravel lot surrounding the vineyard garage and the fallow field separating north and south vineyards (see Figure 2). The reflectance values are being used to evaluate and calibrate the airborne and satellite spectral observations. At the sapflow sites (see Fig. 2), leaf level hyperspectral measurements were made for the same leaves used to measure plant conductance, photosynthetic activity, and leaf water potential to explore relationships between plant physiology and spectral response.

#### IOP micrometeorological observations

During the IOPs, measurements were also collected in the interrow region within the north and south vineyard flux tower footprints to establish micrometeorological conditions between the vine canopies, near the substrate surface. Solar radiation was measured at ground level to determine radiation divergence within the vine canopy. Specifically, solar radiation in the interrow was measured within 75 m of the flux towers during the IOPs using a transect of 5 to 8 radiation sensors from Kipp and Zonen (CMP3 and CMP11, Kipp and Zonen) Eppley (PSP, Eppley Laboratory Inc. Newport Rhode Island, USA) , and Apogee (SP 212, Apogee Instruments Inc. Logan, Utah USA) installed at ground level. Multiple radiometric temperature measurements of the top, east and south facing sides of the vine canopy and the interrow were collected. The two near-nadir viewing sensors at the canopy top (SI-1H1, Apogee Instruments Inc.) were pointed north and south, while two additional Apogee SI-1H1 sensors were angled 90 degrees viewing north and south sides of the vine canopy and two thermal-infrared sensors east facing at an oblique angle viewed the interrow cover crop and bare soil underneath the vines. In 2015, micro-Bowen ratio systems (Holland et al, 2013) were deployed for the three IOPs. There were three micro-Bowen ratio systems located on the north and south facing locations under the

vine canopy sampling the bare soil strip and a third in the center of the interrow. Locations of these measurement sites for both the continuous measurements collected throughout the year and observations collected during IOPs are depicted in Figure 2.

#### IOP UAV acquisitions

Airborne high-resolution (<1m) remote sensing imagery was collected during several of the IOPs in 2013-2016 to evaluate and improve performance of TSEB applications at the satellite pixel scale (30m). In 2013, a manned aircraft collected imagery at nominally 0.1 m pixel resolution in the visible/near-infrared and 0.5 m in the thermal-infrared for 3 IOPs. A detailed description of the processing and analysis of the data is described in Ting et al. (2016). In the 2014-2016 growing season, we moved from manned to unmanned systems, which are easier to deploy and are increasingly used in agricultural monitoring. The UAV system used in GRAPEX and its sensors are described in detail at the USU Aggie Air website (<http://aggieair.usu.edu/>). During the IOPs, the UAV flew at a nominal altitude of 400 m agl, resulting in 0.15 m pixel resolution in the visible and near infrared bands and 0.60 m resolution in the thermal-infrared. Ground control points collected using a survey-grade Trimble RTK GPS with sub-centimeter absolute accuracy were used to georeference the imagery. Ground-based spectral and thermal-infrared measurements of distinct land surface features were used for image calibration. Atmospheric transmissivity was also collected and used to correct at-sensor radiances to surface values.

The manned and unmanned aircraft were employed to capture microscale spatial information concurrent with Landsat overpasses during the IOPs, facilitating detailed comparisons between satellite and aerial information. In addition, both aerial systems were flown approximately an hour after sunrise and during the afternoon, thus providing the opportunity for a more complete description of energy fluxes over the diurnal cycle.

## REMOTE SENSING OF EVAPOTRANSPIRATION

Over the past decades, remote sensing approaches for mapping ET have advanced significantly (Kalma et al. 2008; Wang and Dickinson 2012), particularly surface energy balance methods using TIR observations of LST (Kustas and Anderson 2009). Using LST data from geostationary and polar orbiting satellites, or airborne imaging systems, the Atmosphere-Land Exchange Inverse (ALEXI) modeling framework and associated flux disaggregation technique (DisALEXI) can be used to map ET from global scales for regional water use assessments down to sub-field spatial scales for precision agricultural management (Anderson et al., 2011). Based on the Two-Source (soil and canopy) Energy Balance land-surface representation, ALEXI/DisALEXI provide estimates of E (evaporation) and T (transpiration) partitioning as well as total ET. Using a multi-sensor data fusion methodology, ALEXI/DisALEXI can provide daily ET estimates at field scale resolutions (Camalleri et al. 2013). This modeling system is briefly described below.

### *Two-Source Energy Balance (TSEB) model*

The TSEB land surface energy balance scheme was developed to explicitly account for the differences in aerodynamic coupling between the soil substrate and the canopy layer (Norman et al., 1995). Figure 3 illustrates the basic set of equations used in TSEB to solve for the energy balance of both the soil substrate and vegetation canopy layers. Key inputs are the surface radiometric temperature  $T_{RAD}$  ( $\theta$ ) at a view angle ( $\theta$ ) and the canopy cover fraction ( $f_c$ ) which is related to the leaf area index. The system of equations for the energy balance of the soil/substrate and canopy are solved in parallel with the radiometric temperature balance equation in Figure 3, which partitions  $T_{RAD}$  into effective soil ( $T_s$ ) and canopy ( $T_c$ ) temperatures. As part of this system, the soil ( $R_{soil}$ ) and canopy ( $R_{canopy}$ ) aerodynamic resistances are used compute to sensible

heat fluxes from the soil and canopy surfaces ( $H_s$  and  $H_c$ , respectively). These combine to yield the total sensible heat flux ( $H$ ) determined by the temperature difference between the canopy air space  $T_{AC}$  and the surface layer  $T_A$  and associated surface layer aerodynamic resistance ( $R_{aero}$ ). The soil and canopy temperatures constrain the sensible heat fluxes, net radiation ( $R_N$ ) and soil heat flux ( $G$ ) with the added initial estimate of canopy latent heat flux ( $LE_c$ ) or transpiration based on either the Priestley-Taylor (PT), Penman-Monteith (PM) or light-use efficiency (LUE) parameterization (see Kustas and Norman, 1999, Colaizzi et al., 2014; Anderson et al., 2008). Finally, the latent heat flux from the soil ( $LE_s$ ) is computed as the residual flux.

### ***Regional implementation of the TSEB***

The TSEB land surface scheme is implemented within a regional model called the Atmosphere Land EXchange Inverse (ALEXI) model (Anderson et al., 1997, 2007). The regional ALEXI system exploits the time-differential morning surface temperature signal provided by geostationary satellites to generate coarse regional maps that are reasonably robust to errors in absolute (instantaneous) land surface temperature (LST) retrieval. The associated disaggregation tool (DisALEXI) uses higher resolution imagery from polar orbiting MODIS or Landsat LST or even airborne thermal data, to disaggregate ALEXI fluxes to finer spatial scales. These outputs, which have been validated against surface measurements, provide field scale estimates of crop water use and stress (Anderson et al., 2004; 2007; 2011; 2012).

### ***Multi-sensor data fusion***

The ALEXI/DisALEXI modeling system has been integrated within a data fusion methodology (see Fig. 4a) to combine approximately daily 1km MODIS retrievals with bi-weekly Landsat (sharpened to 30m) resolution retrievals to produce ET datacubes with both high spatial (30m) and temporal (daily) resolution (Camalleri et al., 2013; 2014). The fusion is



performed using the Spatial and Temporal Adaptive Reflectance Fusion Model (STARFM; Gao et al., 2006). STARFM develops spatially distributed weighting factors describing the spectral and spatial relationship between an existing Landsat and MODIS image pairs which are then used to define the disaggregation weighting functions used with the MODIS images on days when Landsat data are not available. A new data fusion procedure under development will utilize higher resolution LST data from the VIIRS satellite (Fig. 4b). ET fusion experiments in different landcover types are described by Cammalleri et al. (2013, 2014), Semmens et al., (2016), Yang et al. (2017a, b), and Sun et al. (2017).

## ANALYSIS AND PRELIMINARY RESULTS

### *Measurements*

#### *Flux and LAI observations*

With the flux towers at the north and south vineyards separated by only a kilometer, there were no significant differences in the meteorological forcings; namely, radiation, rainfall, air temperature, vapor pressure deficit and wind speed. However, we do expect to see differences in surface energy balance components between the north and south vineyards due to differences in irrigation, vine maturity, leaf area, and biomass.

Biomass variations are summarized by IOP in Figure 5, showing averages of ground measurements of vine and cover crop LAI over the years 2013-2016. The cover crop is most active in IOP1; however, sometimes over-irrigation results in lateral water flow into the interrow causing the cover crop to thrive even in June. Over this time period, the total LAI of both the combined vine and cover crop is on the order of 0.5 units higher in the north vineyard during IOP 2 (mid to late June) and IOP 3 (late July to early August).

To more easily visualize and contrast the main temporal dynamics in the surface energy balance at the two sites, monthly daytime fluxes were computed from the daily observations, and

then these monthly fluxes were averaged over the period from 2013 to 2016 to generate normal flux curves associated with each site (Fig 6). These normal curves show little difference in net radiation (RN) between the two sites at the monthly timestep. However, it is apparent that the north vineyard (site 1) with greater biomass than the south (site 2) vineyard has lower sensible heat flux (H) and higher latent heat flux (LE) during the growing season. Most noteworthy is the decrease in H at site 1 during the period of peak incident solar radiation, which is also a period when air temperature and VPD are near their maximum. This is likely due to the higher biomass in site 1 (Fig. 5), with larger evaporative response to VPD and resulting in a depression in H.

The normal G flux curves also show interesting temporal behavior, indicating bimodal peaks: one in March before the vine leaves have emerged, and the second in September after the vines have senesced. The higher values of G at site 1 during March is likely due to more frequent mowing of the cover crop in that field. Bud break normally occurs in mid to late March; consequently, there is very little if any influence on shading from the vines at that time.

#### Soil moisture measurements

Temporal variations in vine and cover crop biomass and associated rooting depths, along with irrigation and evaporative demand, impact patterns in the soil water profile. This is demonstrated in Figure 7, showing evolution in soil moisture observations at 30, 60 and 90 cm depths collected beneath a vine in north vineyard along with precipitation and irrigation events during 2016. The 30 and 60-cm sensors tend to be most responsive to rainfall which largely occurs in the fall, winter, and early spring, while during irrigation events starting in the late spring (May) and much more frequently starting in early summer (June), only the 30-cm shows a response to irrigation (and a few instances with the 60-cm). The response at 30-cm depth in the fall and winter may be caused in part by the interrow cover crop, which remains green and active during these periods. The 60-cm sensor variation in soil moisture is not as dynamic, while the

90-cm moisture sensor registers an increase in moisture after multiple precipitation events in the fall and early winter, presumably when the vines have undergone senescence. Interestingly, the highest moisture values are with the 90-cm sensor from March through May, a period with active cover crop water use and with vines in early development. There is a decline in moisture at all three depths over this time frame, but only the 30-cm sensor responds to the frequent irrigation events starting in June suggesting the vine root zone is mainly in the upper 30 cm. This pattern is similar to other years.

#### Soil moisture-ET relationship

Daily mean soil moisture from the three profile sensors averaged over all depths is compared to measured daily ET from the tower normalized by potential or reference ET ( $ET_0$ ) using the Penman-Monteith equation from FAO56 (Allen et al. 1998) in Figure 8. The daily data come from all four years (2013-2016) are plotted with different symbols indicating different vine phenological and seasonal stages or conditions. Although there is considerable scatter, an exponential equation using a least squares fit indicates a decrease in the ratio of ET to  $ET_0$  starts to occur at a profile soil moisture average of 0.35. However, this depends to some extent on vine phenology. For example, the period from veraison to harvest  $ET/ET_0$  shows little change with average profile of soil moisture decreasing from 0.35 to 0.25. A significantly greater change with daily average soil moisture is observed with changes in  $ET/ET_0$  at the post-harvest stage, while for bud break to bloom or flowering there is little relationship. This lack of a relationship stems from the fact that ET is largely coming from the cover crop in the spring, from prior to and several weeks after bud break and is accessing very little of the available water in the profile underneath the vines.

#### Micro-Bowen ratio and radiation measurements in the interrow

To better understand the microclimate of the vine and interrow system, three micro-Bowen ratio stations were deployed during three IOPs in 2015. Additionally, for all years and IOPs, measurements of solar radiation reaching the ground were made across the vine/interrow system. These measurements will help to improve our understanding of radiation and wind divergence through the canopy layer, and to determine whether the model formulations for below-canopy flux exchange properly account for the unique effects of the vineyard architecture and microclimate (Kool et al., 2016).

An example of the diurnal fluxes from the three micro-Bowen ratio (micro-BR) systems is illustrated in Figure 9, along with a photo and schematic illustrating the measurement design during IOP 2 (June 2015). There is significant spatial and temporal variation in the below-canopy fluxes due primarily to variability in radiation. The micro-BR unit located in the north-facing row underneath the vines receives little radiation over the course of the day and hence produces low fluxes. On the other hand, the micro-BR system under the south facing vine row receives high radiation loading during midday and afternoon periods and yields significant soil heat and latent heat fluxes due to relatively wet soil conditions from the drip irrigation system. Interestingly the micro-BR unit in the center of the interrow yields large deviations in radiation and sensible heat flux values but with little temporal variation and magnitude in soil heat flux. In large part, this is due to a residue layer of senescent cover crop insulating the dry soil in the interrow.

The variation in solar radiation reaching the ground in the interrow and underneath the vines has great spatial and temporal variability as seen in the example from July 11, 2015 in Figure 10, showing radiation measurements from 5 to 8 sensors deployed across the interrow in the north vineyard (site 1) and south vineyard (site 2). These are 15-8minute average radiation values during peak vine cover, and demonstrate that the greater biomass and leaf area of site 1 results in significantly less radiation reaching the ground surface. The heterogeneity in the vine canopy

cover across the interrow results in the lack of a “smooth” sinusoidal radiation curve measured below the vine canopy

#### Sapflow measurements

To evaluate model partitioning of ET into soil evaporation (E) and cover crop and vine transpiration (T), vine sapflow measurements were deployed at several locations in the vineyard to estimate vine T (see Fig. 2). The upscaling of sapflow measurement to canopy level is challenging, and will use LAI data collected in situ along with remote sensing-based estimates of daily LAI described below (Sun et al., 2017). Transpiration estimates from sapflow data will be compared to estimates from a new micrometeorological technique using turbulence data from eddy covariance flux towers which provide E and T at field scale. This method is based on flux-variance similarity theory, and uses parameterized leaf-level water use efficiency and analysis of the correlation structure of high frequency carbon and water vapor concentration time-series observations from each flux averaging interval (Scanlon and Kustas 2010, 2012). A preliminary analysis of the flux partitioning estimates using EC data for the month of June, 2015 yielded a ratio of T to ET of 0.80 from sapflow measurements versus 0.83 from the flux-variance approach. Other months and years during the growing season are currently being analyzed.

#### Surface Renewal

The surface renewal (SR) technique was proposed by Paw U et al. (1995) as a less expensive alternative to EC for estimating sensible heat flux. SR uses a fast response thermocouple near the land surface to analyze the energy budget of air parcels that reside ephemerally within the crop canopy during the turbulent exchange process. The air parcels are manifested as ramp-like shapes in turbulent temperature time series data, and the amplitude and period of the ramps are

used to calculate the sensible heat flux density. With an estimate of  $H$ ,  $LE$  (and therefore  $ET$ ) is computed as the residual of the energy balance equation (top equation in Fig. 3).

In early studies, the SR method required calibration when applied to different land cover conditions (French et al., 2012) using 3D sonic measurements of  $H$ . However, it was recently shown that the calibration factor converges near the theoretically predicted value after compensating for the frequency response characteristics of the SR thermocouple (Shapland et al. 2014). This led to the development of an inexpensive, stand-alone SR method to measure sensible heat flux without the need for EC calibration.

Estimates of  $H$  from the SR station in the south vineyard were computed according to Shapland et al. (2014). The SR estimates of sensible heat flux collected over the 2015 growing season (from April through September) in the south vineyard showed good agreement with EC sensible heat flux (Fig. 11), yielding a least squares regression slope near 1 and a coefficient of determination ( $R^2$ ) of 0.9. For daytime conditions with  $H > 50 \text{ W m}^{-2}$ , the mean absolute percent error (MAPE), calculated as mean absolute error (MAE) divided by mean of the observations multiplied by 100, was 20%. These results are consistent with recent findings showing strong correlation between stand-alone SR, EC and weighing lysimetry in another experimental vineyard (Parry et al. 2017).

## ***Evaluation of canopy formulations***

### ***Radiation divergence within the canopy***

The downwelling shortwave radiation measurements below the vine canopy and across the interrow are being used to evaluate radiation divergence models of varying levels of complexity and methods for computing transmitted solar radiation through the canopy to the ground level. Modeled-measured differences are indicated by the scatter plots for selected models and error

histograms for all models in Figure 12. Models 1 through 3 use Campbell and Norman (1998) radiation transfer model, while model 4 uses the 4-stream Scattering by Arbitrary Inclined Leaves (4SAIL) model (Verhoef et al. 2007) and model 5 uses the Discrete Anisotropic Radiative Transfer (DART) model (Gastellu et al., 1996). Four of the five models being tested (models 2, 3, 4, and 5) account for the unique canopy distribution of the vineyard row structured canopies. Models 2, 3, and 4 use a geometric view factor approach (treating the canopy as either an elliptical or rectangular hedgerow), and model 5 characterizes the canopy as a three-dimensional structure. Model 1, which does not account for the canopy row crop distribution, and uses an empirical clumping index meant for randomly placed canopies such as forests.

While all five models had good agreement with the measured values ( $R^2$  ranging from 0.95 to 0.97), the models that treat row structure with greater geometric fidelity (2-5) showed significant improvement in comparison with the baseline (model 1) based on the error histograms. Of these, model 3 based on Colaizzi et al (2012) and 5 (the most complex DART model) performed best yielding the least bias and lowest overall error.

#### Canopy wind profile model

A new canopy wind profile model proposed by Massman et al. (2017) accommodates non-uniform canopy structure and wind attenuation with depth throughout the canopy. Multi-level within-canopy wind measurements collected during GRAPEX IOPs are being used to investigate whether this new model provides a more physically realistic method for calculating wind speed attenuation for canopies of arbitrary foliage distribution and leaf area. In comparison with previously used canopy wind profiles in TSEB such as Goudriaan (1977) or Massman (1987; 1997), the new method uses an additional input describing the relative canopy foliage vertical distribution. In the case of our study site, the foliage distribution function is considered as a



combination of Gaussian curves representing the foliage for the vine canopy and the cover crop layer underneath.

Preliminary results illustrated in Figure 13 (top row) compares modeled below-canopy wind speed at 1.5 m agl from the new Massman et al. (2017) model and the Goudriaan (1977) uniform-canopy wind model, originally used in TSEB, with measured horizontal wind speed from the 3D sonic anemometer deployed during the 2015 IOPs in the north and south vineyards. The new Massman formulation better reproduces below canopy wind speed measurements in comparison with the Goudriaan approach, improving  $R^2$  from 0.42 and 0.69 at sites 1 and 2, respectively, to 0.54 and 0.76. When embedded within the TSEB, the Massman et al (2016) model improved agreement with measured H fluxes (Fig. 13, bottom row) in comparison with the Goudriaan model, increasing  $R^2$  from 0.6 to 0.7 and reducing daytime MAPE from ~30% to ~20% at both sites.

## ***Evaluation of remote sensing products***

### ***UAV data products***

For the AggieAir flights, an intermediate product from photogrammetric procedures applied to aerial imagery is the estimation of digital surface models (DSM) describing surface topography. Due to the nature of the information (sunlight surface reflection or reflectance), these DSM models provide a topographic description of the illuminated objects in the aerial imagery, and with ground control points provided the DSM accuracy can be close to that of LIDAR products (vertical accuracy < 0.05m).

Canopy volume estimations (Fig. 14) were made for individual vines in the vineyard using the DSM, derived from optical camera images at 0.1 to 0.15 m pixel resolution. To discriminate only canopy volume, a description of the vine spacing and trellis system, bare vine trunk height and survey-grade GPS coordinates of multiple bare soil locations were necessary. In operations,

these canopy volume maps which correlate well with the yield map (Fig. 14) may facilitate identification of dead/unproductive vines and within-season prediction of grape yield and its variability.

The DSM maps also allow detailed analysis of influence of canopy structure and topography on signals recorded by imaging sensors. For example, vegetation oriented away from or towards the sun will appear darker or brighter, respectively, when compared to a horizontal flat surface. This micro-scale sun angle-canopy orientation affects the reflectance and temperature of images, and introduces uncertainty in the analytic results obtained from the imagery (from simple vegetation indices to much more complicated ET or soil moisture estimates). Few studies are found in the literature that use airborne very-high resolution imagery to assess these issues, although correction methods have been developed to reduce the topographic influence on satellite data (e.g., Li et al., 2012 for Landsat-8; Szantoi and Simonetti, 2013 for Landsat 5, 7, and SPOT-5).

Related effects of canopy shadowing introduce another level of complexity to image processing known as shadow identification, de-shadowing, or shadow correction (Fig. 14). Researchers have investigated shadow detection and removal from satellite imagery (e.g., Richter and Muller, 2005; Arevalo et al., 2008). However, there are no analogous procedures developed for detection and removal of shadow affected pixels for high-resolution airborne imagery. The impact of shadowing on ET estimation at high resolution is also being evaluated as part of GRAPEX (Fig. 15).

#### TSEB applications to UAV data

The UAV imagery was used to test performance of the TSEB at very high resolution, similar to the study by Hoffman et al. (2016). The original TSEB version, which assumes the canopy transpires at the Priestley-Taylor rate (Norman et al. 1995) as an initial first approximation

(TSEB-PT), was applied to UAV-acquired thermal radiance data aggregated from the original 0.6 m resolution to 3.6 m – approximately the scale of a single vine-interrow system (3.35 m wide). The sub-meter native resolution of the UAV imagery also allows the retrieval of the component canopy and soil/interrow temperatures that can be used directly in a two-temperature version of TSEB (TSEB-2T; Kustas and Norman, 1997; Colaizzi et al., 2012) which does not require an initial assumption of the canopy transpiration. Comparisons of EC flux observations with flux estimates from each modeling approach, generated using UAV data from 2014 and 2015, are shown in Figure 16.

The TSEB-2T provides improved estimates of H and LE, with a MAE of 30 and 50 W m<sup>-2</sup>, respectively - nearly half of the MAE from TSEB-PT. For LE, the MAPE values were 25% and 15% for TSEB-PT and TSEB-2T, respectively. ET images generated by TSEB-PT and TSEB-2T for a UAV flight in early August of 2014 are illustrated in Figure 17. indicating that both model versions produce similar ET patterns. The tendency is for TSEB-2T to have lower LE values in certain areas within the vineyards, indicating lower vine water use and perhaps some degree of stress. Red areas, with LE close to zero, are found on roads, a paved residential area, and an area between the north and south vineyards comprised of senescent grass. The small rectangular blocks of low ET in the north and south vineyards are protected vernal pools containing grasses and ephemeral wetlands, where vines are not allowed to be planted.

#### Satellite-based leaf area index retrieval

Leaf area index is a key input to TSEB (as well as many other land surface models) and a quantity associated with many biophysical applications (Myneni et al., 2002). Seasonal maps of LAI may also be useful for estimating grape yield in vineyards (Sun et al., 2017). A machine learning approach (Gao et al., 2012) was applied to generate daily LAI maps at 30-m resolution over the GRAPEX field sites using Landsat surface reflectance and the MODIS LAI products. In this approach, the Cubist regression tree software was applied to train LAI and surface

reflectance at the MODIS 1-km resolution. The resulting regression trees were then applied to the 30-m resolution Landsat data to generate LAI maps at Landsat scale (see example in Fig. 17). Comparison of retrieved Landsat LAI with ground LAI measurements in the north and south vineyards from 2013 to 2016 yielded a MAE of 0.44 and a MAPE of ~25% (Sun et al., 2017). An example of the time series in daily LAI estimated from Sun et al (2017) versus the LAI ground sampling in 2014 near the flux towers indicates good agreement (Fig. 18). Also shown is a LAI map for the north and south vineyards at 30 m resolution near the time of peak LAI.

#### Satellite-based ET retrievals

The performance of a prototype ALEXI/DisALEXI/data fusion ET modeling system was evaluated for the 2013 growing season by Semmens et al. (2016), yielding MAE of 0.7 and 0.75 mm/day and MAPE ~19% and 23% in comparison with daily flux observations from the north and south vineyards, respectively. With additional years of data and model improvements based on GRAPEX field observations, model performance has improved, particularly in the ability to recover spring-time evaporative fluxes which are critical to decisions on when to start irrigation. We can now compare daily ET over multiple full annual cycles, yielding MAE values of 0.6 mm/day and MAPE values of 18% for both sites for the period 2013-2016 (Fig. 19). The model will continue to be refined, testing the new formulations for in-canopy wind profile and radiation divergence described above, which are likely to improve agreement with the ET observations. We will also use sapflow-based estimates of vine transpiration to test the E-T partitioning capabilities of TSEB at the 30-m Landsat pixel scale. Additionally, with multiple years of daily ET maps at 30-m resolution, we can begin to investigate changes in water use that are occurring over the landscape due to varying climate as well as changes in land-use and water management strategies (Fig. 19).

## **FUTURE OF GRAPEX**

### ***Domain expansion – capturing the climatic gradient in the Central Valley***

In 2017, the GRAPEX project has extended observations both north (Barrelli vineyard 38.75 N 122.98 W) near Cloverdale CA and south (Rippperdan vineyard 36.84 N 120.21 W) near Madera CA of the current vineyards (Borden Ranch vineyard 38.29 N 121.12 W) near Lodi CA (Figure 19). This network samples a significant north-south climate gradient, with degree day accumulations (DD) for the growing season of 2500 DD for Barrelli, 3700 DD for Borden to 4200 DD for Rippperdan. In addition, three different varieties and trellis designs are used at these sites, providing a wide range in canopy structure and vine physiology for evaluating the land surface scheme of TSEB and the data fusion ET toolkit. For 2017, IOPs were conducted from mid-July to early August (veraison period) when there was high evaporative demand.

### ***Operational applications of technologies***

As the integrated ET toolkit matures, the GRAPEX team will be working with the E&J Gallo Viticulture, Chemistry & Enology and GIS teams, along with growers, to evaluate its utility and application, including modes of effective information transfer and how specific irrigation and water management decisions are to be triggered by this information. In addition, this ET toolkit will be readily available to other commodity groups, particularly high-value perennial crops such as orchards, a major water user in California.

E&J Gallo has estimated that if a more robust ET monitoring system resulted in a 10% reduction in water use for the vineyards in California, there would be considerable economic savings of up to \$200 million based on the value of irrigated water, which in 2014 and 2015 reached \$1,000 or more per acre foot in some parts of California. Pumping costs in 2017 are projected to be around \$150 per acre, so a 10% savings would yield about \$14 million across the entire vineyard acreage of the state.

The GRAPEX project will also help define how UAV data can be integrated into the comprehensive monitoring system, providing important information about the condition of the vines and interrow soil/cover crop, which cannot be discriminated at satellite pixel resolutions. Does having periodic UAV imagery complement the satellite data stream? What are critical times in vine phenology stages (berry formation, veraison, post-veraison berry ripening) when this higher resolution information may be most useful for vineyard management?

## **ACKNOWLEDGEMENTS**

Funding provided by E.&J. Gallo Winery made possible the acquisition and processing of the high-resolution manned aircraft and UAV imagery collected during GRAPEX IOPs. In addition, we would like to thank the staff of Viticulture, Chemistry and Enology Division of E.&J. Gallo Winery for the collection and processing of field data during GRAPEX IOPs. Finally, this project would not have been possible without the cooperation of Mr. Ernie Dosio of Pacific Agri Lands Management, along with the Borden vineyard staff, for logistical support of GRAPEX field and research activities. Finally, the authors would like to acknowledge financial support for this research from NASA Applied Sciences-Water Resources Program [Announcement number NNH16ZDA001N-WATER]. USDA is an equal opportunity provider and employer.

## REFERENCES

- Allen, R. G., L. S. Pereira, , D. Raes, and M. Smith, 1998: Crop evapotranspiration (guidelines for computing crop water requirements), FAO irrigation and drainage paper no.56, FAO, 300 pp.
- Anderson, M.C., J.M. Norman, W.P. Kustas, R.M. Houborg, P.J. Starks, and N.A. Agam, 2008: thermal-based remote sensing technique for routine mapping of land-surface carbon, water and energy fluxes from field to regional scales. *Remote Sens. Environ.*, 112, 4227–4241.
- Anderson, M.C., W.P. Kustas, J.M. Norman, C.R. Hain, J.R. Mecikalski, L. Schultz, M.P. Gonzalez-Dugo, C. Cammalleri, G. d'Urso, A. Pimstein, and F. Gao, 2011: Mapping daily evapotranspiration at field to continental scales using geostationary and polar orbiting satellite imagery. *Hydrol. Earth Syst. Sci.*, 15, 223-239.
- Anderson, M.C., R.G. Allen, A. Morse, and W.P. Kustas, 2012: Use of Landsat thermal imagery in monitoring evapotranspiration and managing water resources. *Remote Sens. Environ.*, 122, 50-65.
- Anderson, M.C., J.M. Norman, J.R. Mecikalski, R.D. Torn, W.P. Kustas, and J.B. Basara, 2004: A multi-scale remote sensing model for disaggregating regional fluxes to micrometeorological scales. *J. Hydrometeor.*, 5, 343-363.
- Anderson, M.C., J.M. Norman, J.R. Mecikalski, J. Otkin, and W.P. Kustas, 2007: A climatological study of evapotranspiration and moisture stress across the continental U.S. based on thermal remote sensing: I. Model formulation. *J. Geophys. Res.*, 112, D10117, doi:10.1029/2006JD007506.
- Arevalo V., J. González, and G. Ambrosio, 2008: Shadow detection in colour high-resolution satellite images. *Inter. J. Remote Sens.*, 29(7), 1945–1963. doi: 10.1080/014311 60701395302
- Bellvert J., J. Marsal, J. Girona, P. J. Zarco-Tejada, 2015: Seasonal evolution of crop water stress index in grapevine varieties determined with high-resolution remote sensing thermal imagery *Irrig Sci.*, 33:81–93.
- Bellvert J, P. Zarco-Tejada, J. Marsal, J.Girona, V. Gonzalez-Dugo E. Fereres 2016: Vineyard irrigation scheduling based on airborne thermal imagery and water potential thresholds. *Aus. J. Grape Wine Res.* 22(2):307-315.
- Cammalleri, C., M.C. Anderson, G. Ciraolo, G. D'Urso, W.P. Kustas, G. La Loggia, and M. Minacapilli, 2010: The impact of in-canopy wind profile formulations on heat flux estimation in an open orchard canopy using the remote sensing-based two-source model. *Hydrol. Earth Syst. Sci.*, 14, 2643-2659



Cammalleri, C., M.C. Anderson, F. Gao, C.R. Hain, and W.P. Kustas, 2013: A data fusion approach for mapping daily evapotranspiration at field scale. *Water Resour. Res.*, 49(8), 4672-4686.

Cammalleri, C., M.C. Anderson, F. Gao, C.R. Hain, and W.P. Kustas, 2014: Mapping daily evapotranspiration at field scales over rainfed and irrigated agricultural areas using remote sensing data fusion. *Agri. Forest Met.*, 186, 1-11.

Campbell, G. S. and J.M. Norman 1998: *An Introduction to Environmental Biophysics* Springer-Verlag New York, New York, 2nd edition, 286 pp.

Colaizzi, P.D., S.A. O'Shaughnessy, P.H. Gowda, W.P. Kustas, M.C. Anderson, S.R. Evett, and T.A. Howell, 2010: Radiometer footprint model to estimate sunlit and shaded components for row crops. *Agron. J.*, 102, 942-955.

Colaizzi, P.D., S.R. Evett, T.A. Howell, F. Li, W.P. Kustas, and M.C. Anderson, 2012: Radiation model for row crops: I. Geometric view factors and parameter optimization. *Agron. J.*, 104, 225-240.

Colaizzi, P. D., N. Agam, J.A. Tolck, S.R. Evett, T.A. Howell, P.H. Gowda, S.A. O'Shaughnessy, W.P. Kustas, and M.C. Anderson, 2014: Two-source energy balance model to calculate E, T, and ET: Comparison of Priestley-Taylor and Penman-Monteith formulations and two time scaling methods. *Trans. ASABE*, 57(2), 479-498. <http://dx.doi.org/10.13031/trans.57.10423>.

Colaizzi, P. D., W.P. Kustas, M.C. Anderson, N. Agam, J.A. Tolck, S.R. Evett, T.A. Howell, P.H. Gowda, and S.A. O'Shaughnessy, 2012: Two-source energy balance model estimates of evapotranspiration using component and composite surface temperatures. *Adv. Water Resour.*, 50, 134-151. <http://dx.doi.org/10.1016/j.advwatres.2012.06.004>.

Colaizzi, P. D., N. Agam, J.A. Tolck, S.R. Evett, T.A. Howell, S.A. O'Shaughnessy, P.H. Gowda, W.P. Kustas, and M.C. Anderson, 2016: Advances in a two-source energy balance model : Partitioning of evaporation and transpiration for cotton using component and composite surface temperatures. *Trans. ASABE*, 59(1), 181-197. Doi 10.13031/trans.59.11215.

French A.N., J.G. Alfieri, W.P. Kustas, J.H. Prueger, L.E. Hipps, J.L. Chávez, S.R. Evett, T.A. Howell, P.H. Gowda, D. Hunsaker, and K. Thorp 2012: Estimation of surface energy fluxes using surface renewal and flux variance techniques over an advective irrigated agricultural site. *Adv. Water Resour.*, 50, 91-105.

Gao, F., J. Masek, M. Schwaller, and F.G. Hall, 2006: On the blending of the Landsat and MODIS surface reflectance: predicting daily Landsat surface reflectance. *IEE Trans. Geosci. Remote. Sens.*, 44, 2207-2218.

Gao, F., M.C. Anderson, W.P. Kustas, and Y. Wang, 2012: A simple method for retrieving Leaf Area Index from Landsat using MODIS LAI products as reference. *J. Appl. Remote Sens.*, 6, DOI: 10.1117/JRS.1116.063554

Gao, F., T. Hilker, X. Zhu, M.C. Anderson, J. Masek, P. Wang, and Y. Yang: 2015, Fusing Landsat and MODIS data for vegetation monitoring. *IEEE Geosci. Remote Sens. Mag.*, 3, 47-60.

Gao, F., M.C. Anderson, X. Zhang, Z. Yang, J.G. Alfieri, W.P. Kustas, R. Mueller, D. Johnson, and J.H. Prueger, 2017: Toward mapping crop progress at field scales using Landsat and MODIS imagery. *Remote Sens. Environ.*, 188, 9-25.

Gastellu-Etchegorry, J. P., V. Demarez, V. Pinel, and F. Zagolski 1996: Modeling radiative transfer in heterogeneous 3D vegetation canopies. *Remote Sens. Environ.*, 58(2) 131–156.

Goudriaan, J., 1977: Crop micrometeorology: A simulation study. Technical report, Center for Agricultural Publications and Documentation, Wageningen, The Netherlands. Publisher: H. Veenman en Zonen B.V., Wageningen. 247 pp.

Hoffmann, H., H. Nieto, R. Jensen, R. Guzinski, P. Zarco-Tejada, and T. Friborg, 2016: Estimating evaporation with thermal UAV data and two-source energy balance models. *Hydrol. Earth Syst. Sci.*, 20, 697-713.

Holland, S., J.L. Heitman, A. Howard, T.J. Sauer, W. Giese, A. Ben-Gal, N. Agam, D. Kool, and J. Havlin, 2013: Micro-Bowen ratio system for measuring evapotranspiration in a vineyard interrow. *Agric. For. Meteorol.*, 177, 93-100.

Kalma, J.D., T.R. McVicar, and M.F. McCabe, 2008: Estimating land surface evaporation: A review of methods using remotely sensing surface temperature data. *Survey Geophys.*, DOI 10.1007/s10712-10008-19037-z

Kool, D., W.P. Kustas, A. Ben-Gal, N. Lazarovitch, J.L. Heitman, T.J. Sauer, and N. Agam, 2016: Energy and evapotranspiration partitioning in a desert vineyard *Agric. For. Meteorol.*, 218–219, 277–287.

Kustas, W. P., and J.M. Norman, 1997: A two-source approach for estimating turbulent fluxes using multiple angle thermal infrared observations. *Water Resour. Res.* 33:1495-1508. 1997.

Kustas, W. P., and J.M. Norman, 1999: Evaluation of soil and vegetation heat flux predictions using a simple two-source model with radiometric temperatures for partial canopy cover. *Agric. For. Meteorol.*, 94,13-29.

- Kustas, W.P., and M.C. Anderson, 2009: Advances in thermal infrared remote sensing for land surface modeling. *Agric. For. Meteorol.*, 149, 2071-2081.
- Li, F., D. Jupp, M. Thankappan, L. Lymburner, N. Mueller, and A. Lewis, 2012: A physics-based atmospheric and BRDF correction for Landsat data over mountainous terrain. *Rem. Sens. Environ.*, 124, 756–770
- Massman, W.J., 1987: A comparative study of some mathematical models of the mean wind structure and aerodynamic drag of plant canopies. *Bound-Layer Meteorol.*, 40(1), 179–197.
- Massman, W.J., 1997: An analytical one-dimensional model of momentum transfer by vegetation of arbitrary structure. *Bound.-Layer Meteorol.*, 83, 407–421.
- Massman, W.J., J.M. Forthofer, and M.A. Finney, 2017: An improved canopy wind model for predicting wind adjustment factors and wildland fire behavior. *Canadian J. For. Res.* 47, 594-603. doi:10.1139/cjfr-2016-0354
- McElrone, A.J., T.M. Shapland, A. Calderon, L. Fitzmaurice, K.T. Paw U, and R.L. Snyder, 2013: Surface renewal: An advanced micrometeorological method for measuring and processing field-scale energy flux density data. *J. Vis. Exp.* (82), e50666, doi:10.3791/50666.
- Myneni, R.B. S. Hoffman, Y. Knyazikhin, J.L. Privette, J. Glassy, Y. Tian, Y. Wang, X. Song, Y. Zhang, G.R. Smith, G.R.; et al. 2002: Global products of vegetation leaf area and fraction absorbed PAR from year one of MODIS data. *Remote Sens. Environ.*, 83, 214–231.
- Norman, J.M., W.P. Kustas, and K.S. Humes, 1995: A two-source approach for estimating soil and vegetation energy fluxes from observations of directional radiometric surface temperature. *Agric. For. Meteorol.*, 77, 263-293.
- Richter R, and A. Muller 2005: De-shadowing of satellite/airborne imagery. *Inter. J. Remote Sens.*, 26(15), 3137–3148. doi: 10.1080/01431160500114664
- Scanlon, T.M., and W.P. Kustas, 2010: Partitioning carbon dioxide and water vapor fluxes using correlation analysis. *Agric. For. Meteorol.*, 150, 89-99
- Scanlon, T.M., and W.P. Kustas, 2012: Partitioning evapotranspiration using an eddy covariance-based technique: Improved assessment of soil moisture and land-atmosphere exchange dynamics. *Vadose Zone J.*, 11, DOI: 10.2136/vzj2012.0025
- Semmens, K.A., M.C. Anderson, W.P. Kustas, F. Gao, F., J.G. Alfieri, L. McKee, J.H. Prueger, C.R. Hain, C. Cammalleri, Y. Yang, T. Xia, L. Sanchez, M. Mar Alsina, and M. Vélez, 2016: Monitoring daily evapotranspiration over two California vineyards using Landsat 8 in a multi-

sensor data fusion approach. *Rem. Sens. Environ.*, 185, 155-170.  
doi:10.1016/j.rse.2015.1010.1025

Sun, L., Anderson, M.C., Gao, F., Hain, C., Alfieri, J.G., Sharifi, Amir, McCarty, G.W., Yang, Yun, Yang, Yang, Kustas, W.P., McKee, L.G. 2017. Investigating water use over the Choptank River Watershed using a multi-satellite data fusion approach. *Water Resour. Res.* doi 10.1002/2017WR020700 (in press).

Sun, L., F. Gao, M.C. Anderson, W.P. Kustas, M. Alsina, L. Sanchez, B. Sams, L.G. McKee, W.P. Dulaney, A. White, J.G. Alfieri, J.H. Prueger, F. Melton, and K. Post, 2017: Daily mapping of 30 m LAI, NDVI for grape yield prediction in California vineyard. *Rem. Sens.*, 9, 317; 18 pp. doi:10.3390/rs9040317

Shapland, T.M., R.L. Snyder, K.T. Paw U, A.J. McElrone, 2014: Thermocouple frequency response compensation leads to convergence of the surface renewal alpha calibration. *Agric. For. Meteorol.*, 189–190, 36–47.

Szantoi Z., and D. Simonetti, 2013: Fast and robust topographic correction method for medium resolution satellite imagery using a stratified approach. *IEEE J. Sel. Topics Appl. Earth Obs. Rem. Sens.*, 6(4).

Parry, C., A. Calderon, K.T. Paw U, T. Shapland, R. Snyder, A.J. McElrone, 2017: **(In Review)** Comparison of a stand-alone surface renewal method to weighing lysimetry and eddy covariance for determining vineyard evapotranspiration and vine water stress. *Agric. For. Meteorol.*

Paw U, K.T., J. Qiu H.B. Su, T. Watanabe, and Y. Brunet, 1995: Surface renewal analysis: a new method to obtain scalar fluxes without velocity data. *Agric For Meteorol.*, 74,119–137.

Ting, X., W.P. Kustas, M.C. Anderson, J.G. Alfieri, F. Gao, L.G. McKee, J.H. Prueger, H. Geli, C. Neale, L. Sanchez, M. Alsina, and Z. Wang, 2016: Mapping evapotranspiration with high resolution aircraft imagery over vineyards using one and two source modeling schemes *Hydrol. Earth Syst. Sci.*, 20,1523-1545.

Verhoef, W., L. Jia, Q. Xiao, and Z. Su, 2007: Unified optical-thermal four-stream radiative transfer theory. *IEEE Tran. Geo. Remote Sens.* 45 (6):1808-1822.

Wang, K., and R.E. Dickinson, 2012: A review of global terrestrial evapotranspiration: Observation, modeling, climatology, and climatic variability. *Rev. Geophys.*, 50, DOI: 10.1029/2011RG000373

Yang, Y., M.C. Anderson, F. Gao, C. R. Hain, K. Semmens, W.P. Kustas, A. Noormets, R.H. Wynne, V.A. Thomas, and G. Sun, 2017a: Daily Landsat-scale evapotranspiration estimation

844 over a managed pine plantation in North Carolina, USA using multi-satellite data fusion, Hydrol.  
845 Earth Syst. Sci., 21,1017-1037. doi:10.5194/hess-21-1017-2017.  
846  
847 Yang, Y, M.C. Anderson, F. Gao, C.R. Hain, W.P. Kustas, T. Meyers, W.T. Crow, R.  
848 Finocchiaro, J. Otkin, L. Sun, and Y. Yang, 2017b: Impact of tile drainage on  
849 evapotranspiration in South Dakota, USA based on high spatiotemporal resolution ET timeseries  
850 from a multi-satellite data fusion system IEEE J. Selected Topics Appl. Earth Obs. Rem. Sens.  
851 PP(99 ) pp. 1-15. DOI: 10.1109/JSTARS.2017.2680411

## FIGURE CAPTION LIST

Figure 1. (a) A county level map of California gives the location of the Pinot noir vineyards in Sacramento County along with a Landsat 8 Normalized Difference Vegetation Index (NDVI) map showing the location of the vineyards (with yellow boundaries) and with solid yellow circles indicating the approximate location of the flux towers. (b) The photos of the vine and cover crop are indicative of their phenology during the Intensive Observation Periods (IOPs) involving an extensive set of ground and airborne measurements (see text). (c) The vine trellis and interrow cropping design and dimensions are illustrated and listed, respectively.

Figure 2. (a) A photo of the tower installation and sensor locations on the tower is provided, along with (b) a schematic of the soil heat flux sensor measurement design (see text for details). (c) GRAPEX sensor locations in north (site 1) and south (site 2) vineyards, along with leaf area sampling locations during the IOPs.

Figure 3. Schematic diagram of the Two-Source Energy Balance (TSEB) model resistance network for sensible heat flux and the basic set of equations used to obtain an iterative solution. Symbols represent the following: net radiation ( $R_N$ ), soil heat flux ( $G$ ), sensible heat flux ( $H$ ), latent heat flux ( $LE$ ), temperature ( $T$ ), subscripts C and S refer crop and soil/substrate, respectively, radiometric surface temperature ( $T_{RAD}$ ), radiometer viewing angle ( $\theta$ ), fraction vegetation cover ( $f_C$ ), soil/substrate aerodynamic resistance ( $R_S$ ), canopy aerodynamic resistance ( $R_{Cy}$ ), surface layer aerodynamic resistance ( $R_A$ ), canopy-air temperature ( $T_{AC}$ ), and surface layer air temperature ( $T_A$ ). To achieve an iterative solution TSEB initially computes canopy transpiration or canopy latent heat flux ( $LE_C$ ) using Priestley-Taylor (PT), Penman-Monteith (PM) or Light Use efficiency (LUE) formulation.

Figure 4. A schematic overview of the inputs and processing steps of the ET data fusion package for the current processing method and the new processing method under development.

Figure 5. Average of the ground-based LAI measurements near the flux towers collected from the GRAPEX IOPs over the 2013-2016 growing seasons in the north (site 1) and south (site 2) vineyards. Also shown is the additional LAI contributed by the cover crop when active and growing early in the spring and early summer.

Figure 6. Daytime monthly average (mean of 2013-2016) surface energy balance components- net radiation (RN), soil heat flux (G), sensible heat flux (H) and latent heat flux (LE) for north (site 1; solid line) and south (site 2; dashed line) vineyard.

Figure 7. Soil moisture from the -30, -60 and -90 cm profile sensors located underneath a vine for the north (site 1) vineyard in 2016 along with observations of precipitation (mm) and irrigation (mm/vine).

Figure 8. A comparison of profile average daily soil moisture versus ratio of actual to potential ET ( $ET/ET_0$ ) for 2013-2016. The symbols represent data from different vine phenological stages. The curve is an exponential least squares fit through all the data.

Figure 9. The surface energy balance components (top) for a day during IOP2 in June, 2015 as measured by micro-BR systems located under the vines in bare soil area for the north facing vine row (the vine row south of the center of the interrow), for the interrow and for a south facing vine row (the vine row north of the center of the interrow). Additionally, a schematic with photo (bottom) illustrating the micro-BR deployment and measurement design.



902

903 Figure 10. Diurnal radiation measurements above and below the vine canopy using 5 to 8  
904 radiation sensors at north (site 1) and south (site 2) vineyard, respectively, for a clear day during  
905 IOP 3 (July 11) in 2015.

906

907 Figure 11. Hourly sensible heat flux (H) from eddy covariance measured at the south (site 2)  
908 vineyard flux tower, and hourly H from the stand-alone surface renewal for the 2015 growing  
909 season. Dashed line indicates perfect agreement (1:1 line).

910

911 Figure 12. Comparison of solar radiation divergence model estimates with different levels of  
912 complexity (models 1-5) versus the below vine canopy solar radiation measurements (15 min  
913 averages). Error histograms for all the models indicate the least bias and smallest error with the  
914 observations are from using models 3 and 5. Scatter plots for models 3 and 5 are provided with  
915 dashed grey line indicating perfect agreement with observations (1:1 line).

916

917 Figure 13. Comparison of (top) measured 1.5 m wind speeds versus TSEB values (15 min  
918 averages) derived using the Goudriaan and Massman within-canopy wind extinction  
919 formulations for the north and south vineyards (sites 1 and 2), and (bottom) resulting impact on  
920 daytime-integrated sensible heat flux estimates over the 2015 growing season. Dashed line  
921 represents perfect agreement with the observations (1:1 line).

922

923 Figure 14. Example of canopy volume estimated for individual vines for an AggieAir UAV  
924 flight in August 2014 and the 2014 yield map the north vineyard. Note the variability in canopy  
925 volume across the field and an area of highly stressed or dead vines in the upper left with little or  
926 no biomass.

927

928 Figure 15. (Top) Variation in modeled ET due to shadow/micro-topography effects, generated  
929 using a DSM for a vine row viewed at different angles. Black/grey dots are the point cloud data.  
930 (Bottom) Automated identification of shadow locations (light green color) along several rows  
931 overlay red-blue-green (RGB) and near-infrared (NIR) false color UAV imagery.

932

933 Figure 16. Comparison of TSEB flux estimates with energy balance components (net radiation  
934 (RN), soil heat (G), sensible heat (H) and latent heat (LE)) measured at the time of UAV  
935 overpass during flights in 2014 and 2015. Model results are shown (left) using composite  
936 temperatures and TSEB-PT, and (right) using component temperatures and TSEB-2T. In both  
937 cases, the TSEB models were modified to account for radiation and wind transmission through  
938 row crops.

939

940 Figure 17. Latent heat fluxes (LE) maps at 3.5 m resolution computed using TSEB-PT and  
941 TSEB-2T from the UAV imagery collected at the time of Landsat overpass on August 9, 2014.

942

943 Figure 18. On the left is a map of LAI at 30 m resolution for north and south vineyards within  
944 the yellow boundaries at around peak LAI for year 2014 growing season while on the right a  
945 comparison of ground measured versus satellite derived daily LAI near the flux towers in north  
946 and south vineyards over the 2014 growing season (see Sun et al., 2017 for details).

947

948 Figure 19. Cumulative ET (mm) map at 30 m resolution over the growing season (March 1-  
949 September 1) for a 9 x 9 km area surrounding the north and south GRAPEX vineyards (top) and  
950 daily ET modeled over the estimated tower footprint (black line) as well as the maximum and

minimum (range) in ET versus observed (red dots) for the north (site 1) and south (site 2) vineyards (bottom).

Figure 20. The expansion of 2017 GRAPEX experimental vineyard sites from Borden site to Barrelli vineyard to the north and Ripperdan vineyard to the south spanning a large range in degree day accumulations (see text) and vine varieties and trellis designs.

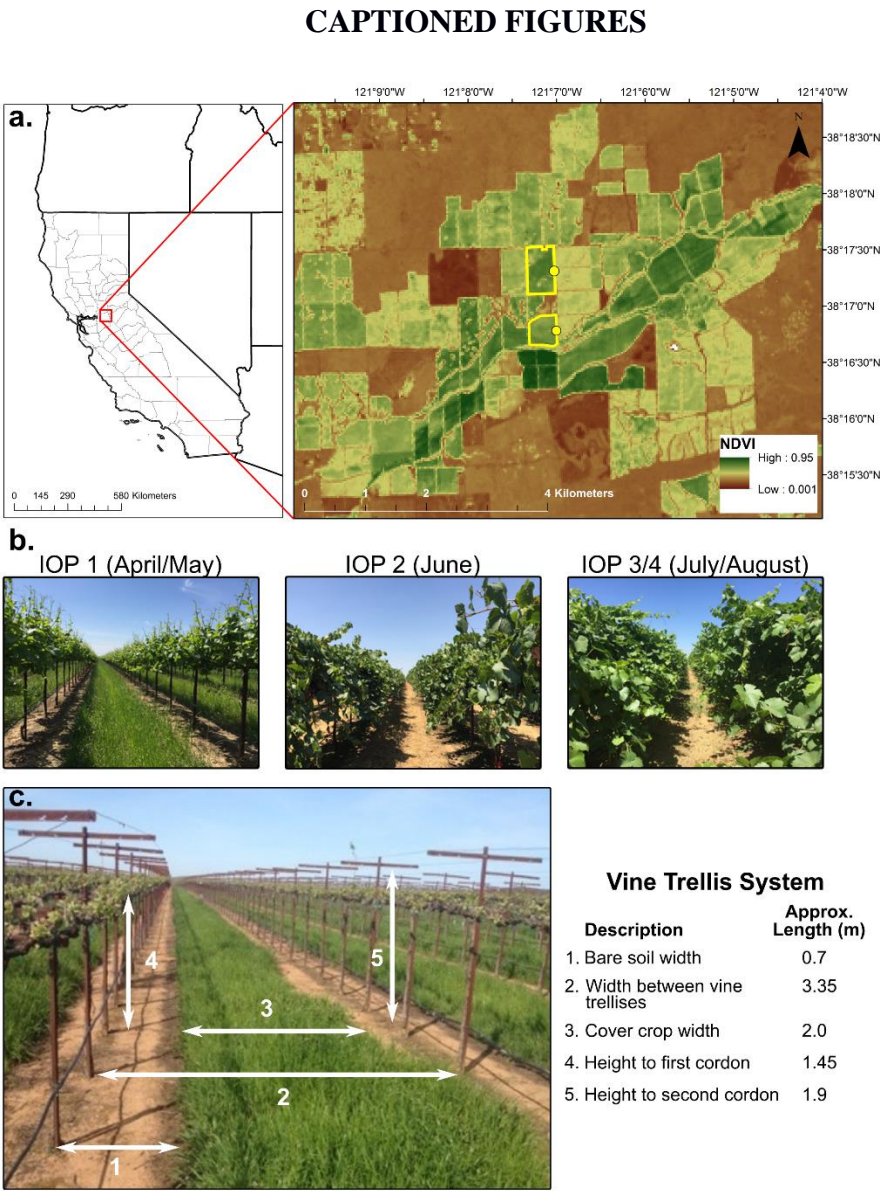


Figure 1. (a) A county level map of California gives the location of the Pinot noir vineyards in Sacramento County along with a Landsat 8 Normalized Difference Vegetation Index (NDVI) map showing the location of the vineyards (with yellow boundaries) and with solid yellow circles indicating the approximate location of the flux towers. (b) The photos of the vine and cover crop are indicative of their phenology during the Intensive Observation Periods (IOPs) involving an extensive set of ground and airborne measurements (see text). (c) The vine trellis and interrow cropping design and dimensions are illustrated and listed, respectively. .

39  
40  
41  
42  
43  
44  
45  
46  
47  
48  
49  
50  
51  
52  
53  
54  
55  
56  
57  
58  
59  
60  
61  
62  
63  
64  
65  
66  
67  
68  
69  
70  
71  
72  
73

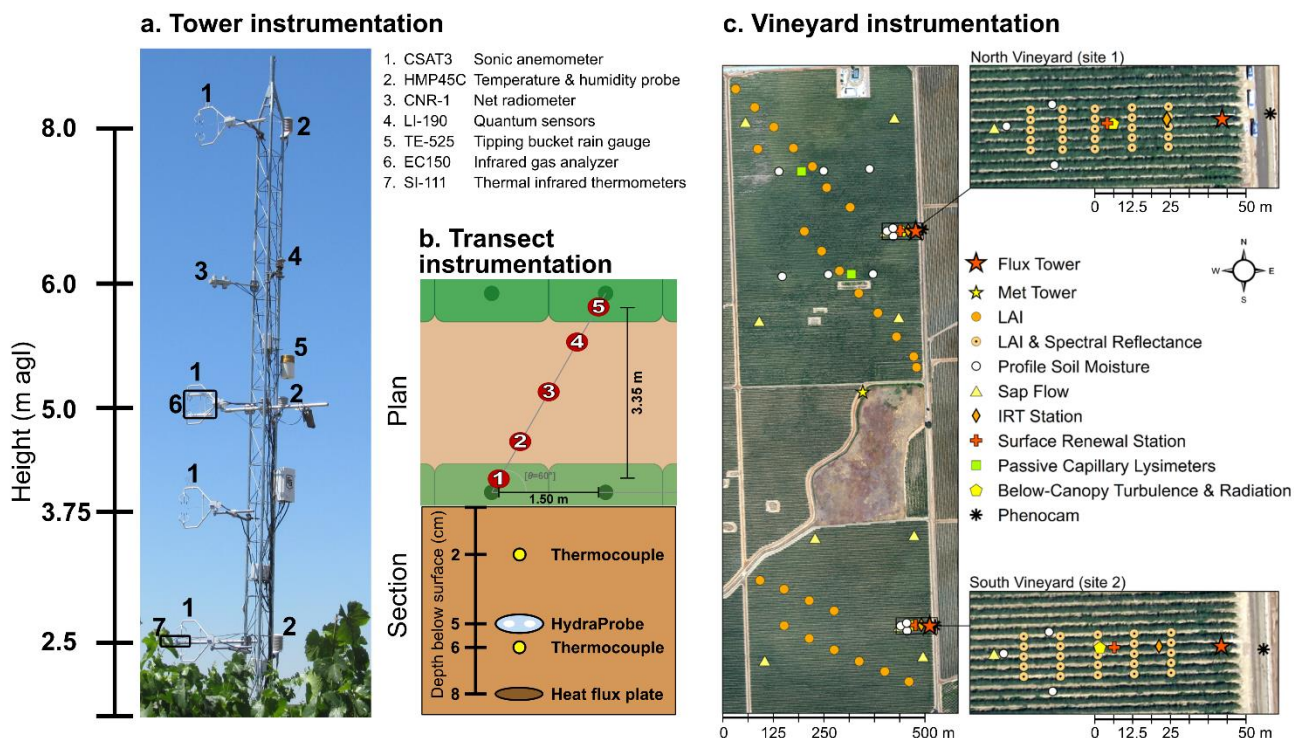
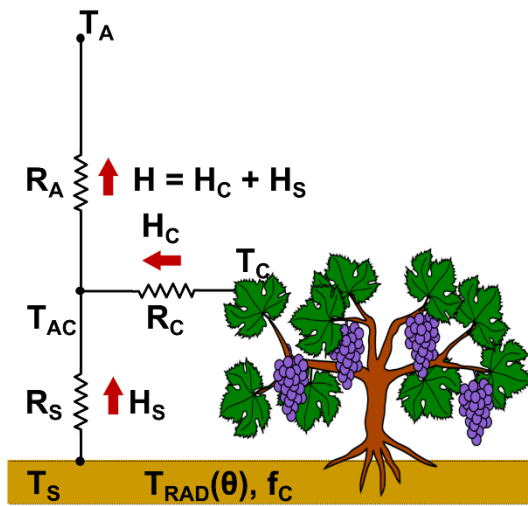


Figure 2 . (a) A photo of the tower installation and sensor locations on the tower is provided, along with (b) a schematic of the soil heat flux sensor measurement design (see text for details). (c) GRAPEX sensor locations in north (site 1) and south (site 2) vineyards, along with leaf area sampling locations during the IOPs.



**Sensible heat flux module**

**System, soil (S), canopy (C) budgets**

$$RN = H + LE + G$$

$$RN_S = H_S + LE_S + G$$

$$RN_C = H_C + LE_C$$

**Two-source approximation**

$$T_{RAD}(\theta)^4 \approx f_C(\theta)T_C^4 + (1 - f_C(\theta))T_S^4$$

**Temperature constraint**

$$H_C, H_S, RN_C, RN_S, G$$

**PT, PM, or LUE  $R_C$  model**

$$LE_C$$

**Residual**

$$LE_S = RN - H - G - LE_C$$

**Iterative energy balance solution**

Figure 3. Schematic diagram of the Two-Source Energy Balance (TSEB) model resistance network for sensible heat flux and the basic set of equations used to obtain an iterative solution. Symbols represent the following: net radiation (RN), soil heat flux (G), sensible heat flux (H), latent heat flux (LE), temperature (T), subscripts C and S refer crop and soil/substrate, respectively, radiometric surface temperature ( $T_{RAD}$ ), radiometer viewing angle ( $\theta$ ), fraction vegetation cover ( $f_C$ ), soil/substrate aerodynamic resistance ( $R_S$ ), canopy aerodynamic resistance ( $R_C$ ), surface layer aerodynamic resistance ( $R_A$ ), canopy-air temperature ( $T_{AC}$ ), and surface layer air temperature ( $T_A$ ). To achieve an iterative solution TSEB initially computes canopy transpiration or canopy latent heat flux ( $LE_C$ ) using Priestley-Taylor (PT), Penman-Monteith (PM) or Light Use efficiency (LUE) formulation.



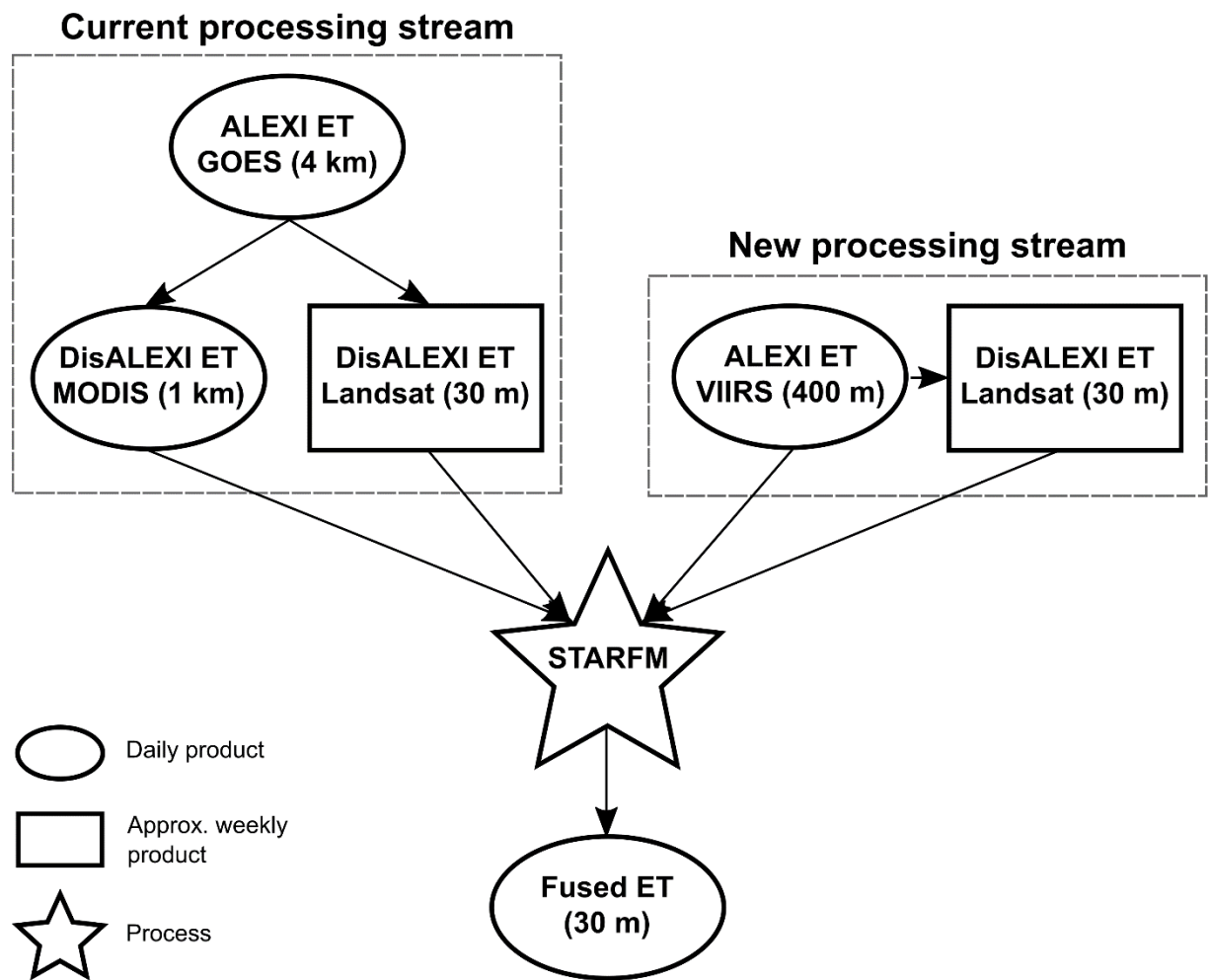


Figure 4. A schematic overview of the inputs and processing steps of the ET data fusion package for the current processing method and the new processing method under development.

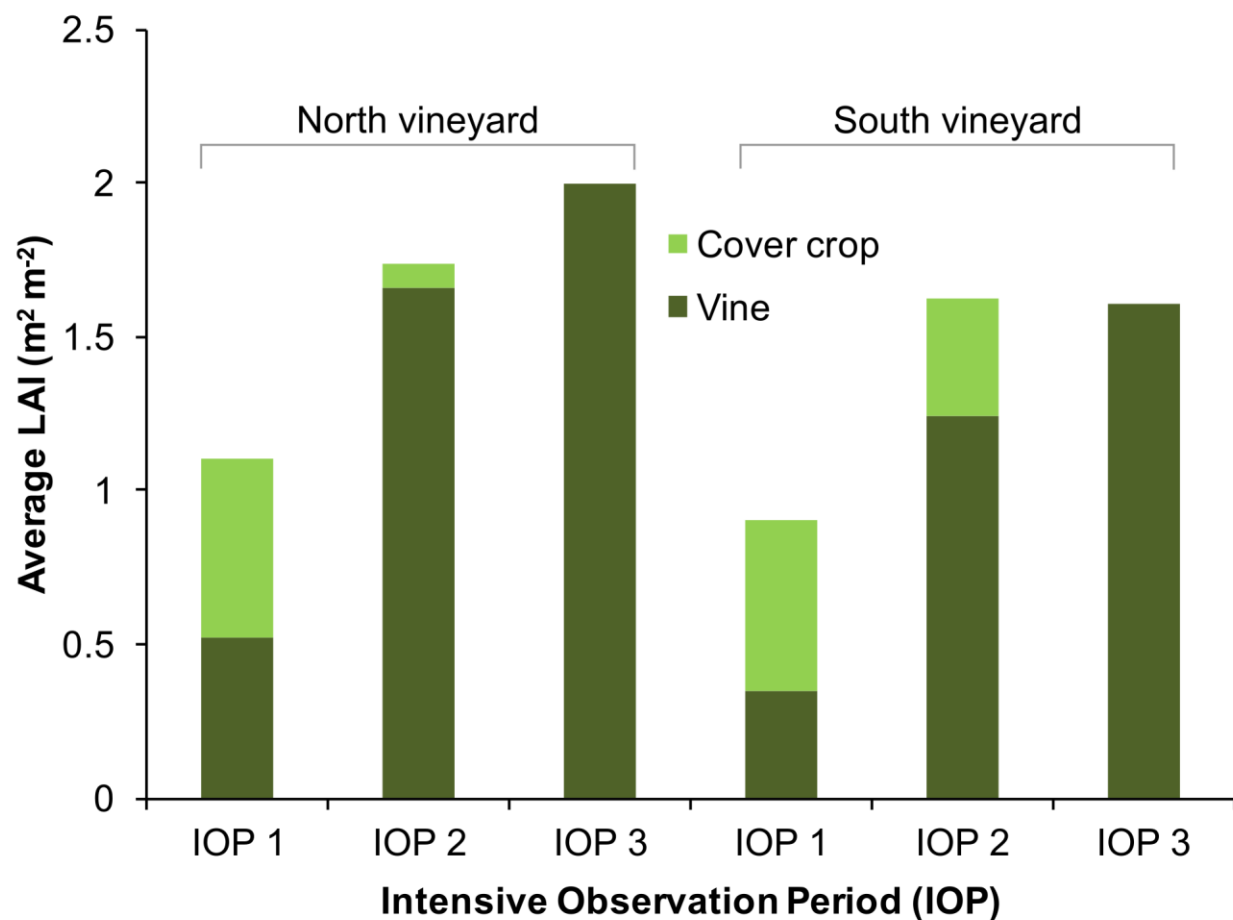


Figure 5. Average of the ground-based LAI measurements near the flux towers collected from the GRAPEX IOPs over the 2013-2016 growing seasons in the north (site 1) and south (site 2) vineyards. Also shown is the additional LAI contributed by the cover crop when active and growing early in the spring and early summer.



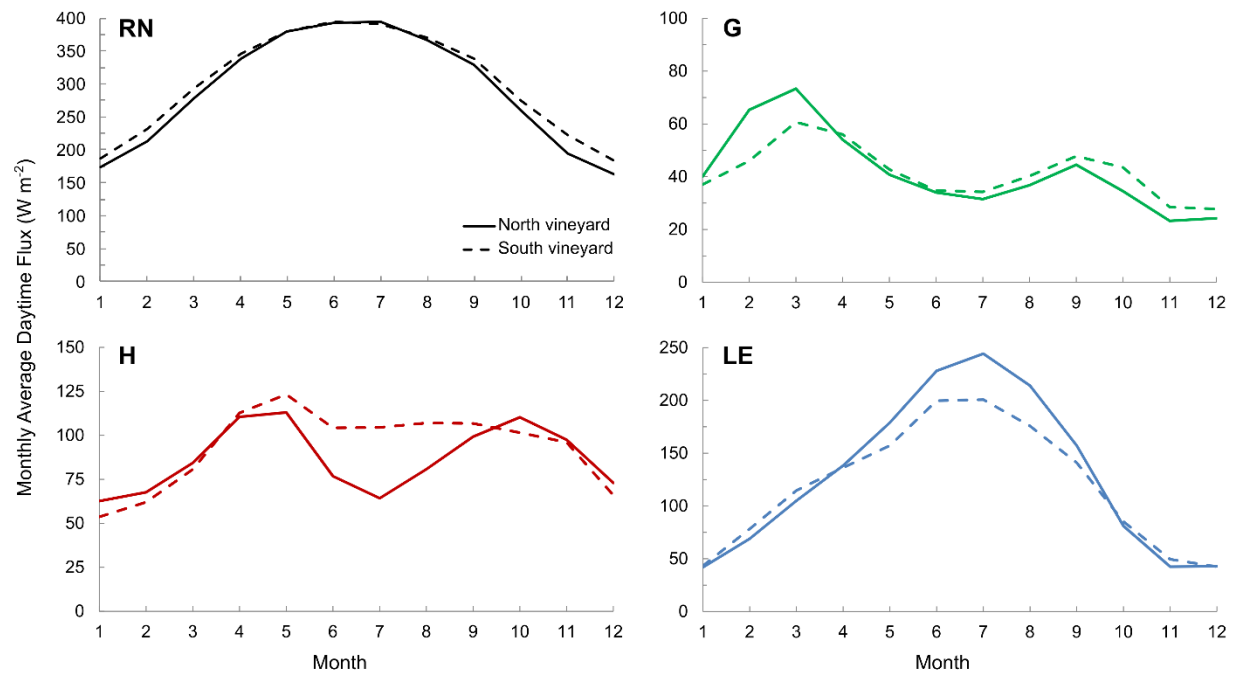


Figure 6. Daytime monthly average (mean of 2013-2016) surface energy balance components- net radiation (RN), soil heat flux (G), sensible heat flux (H) and latent heat flux (LE) for north (site 1; solid line) and south (site 2; dashed line) vineyard.

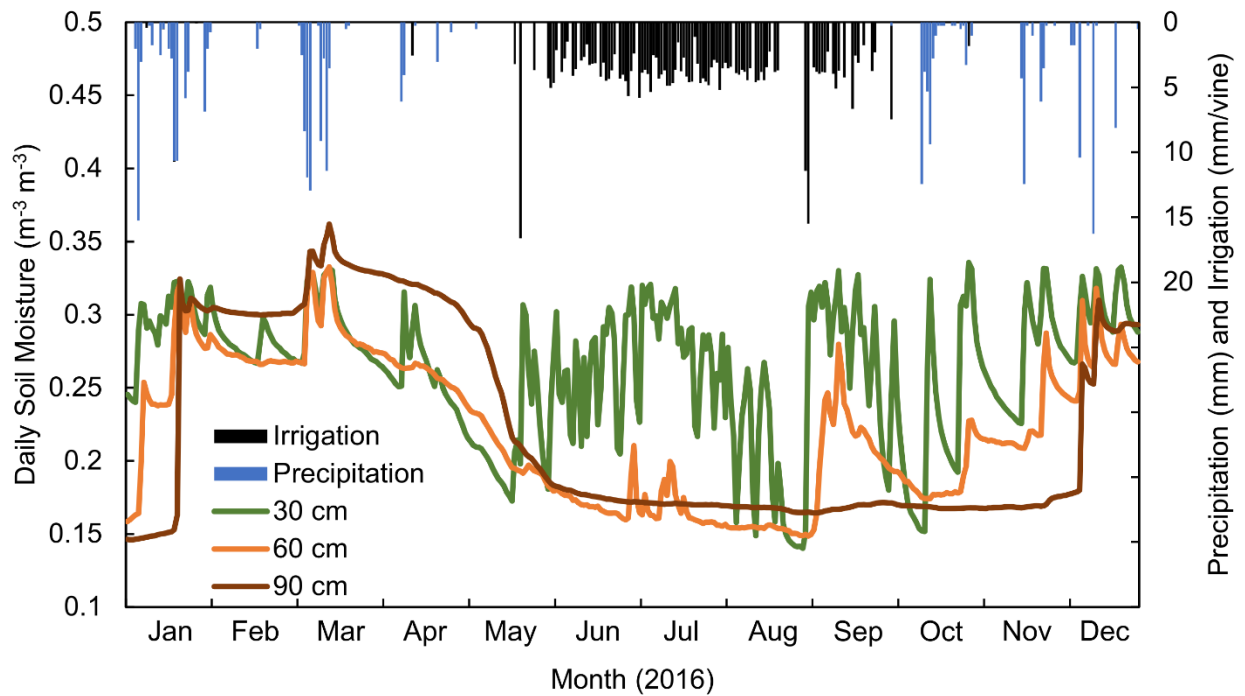


Figure 7. Soil moisture from the -30, -60 and -90 cm profile sensors located underneath a vine for the north (site 1) vineyard in 2016 along with observations of precipitation (mm) and irrigation (mm/vine).

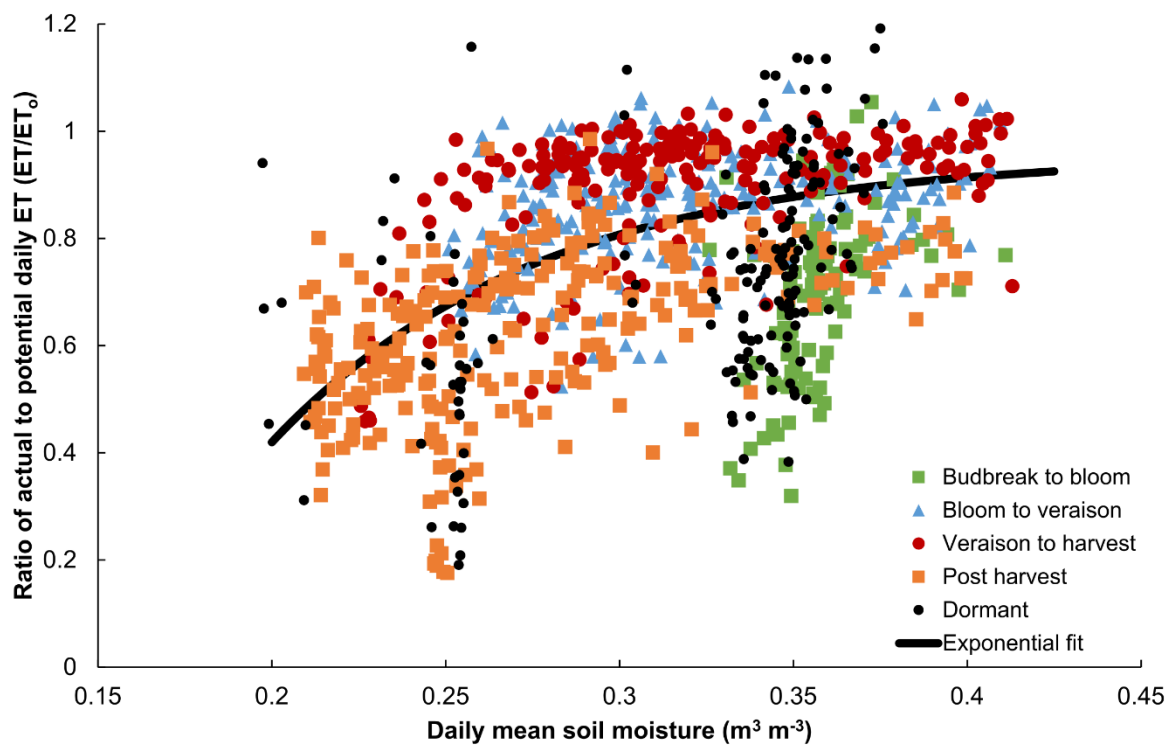


Figure 8. A comparison of profile average daily soil moisture versus ratio of actual to potential ET (ET/ET<sub>0</sub>) for 2013-2016. The symbols represent data from different vine phenological stages. The curve is an exponential least squares fit through all the data.

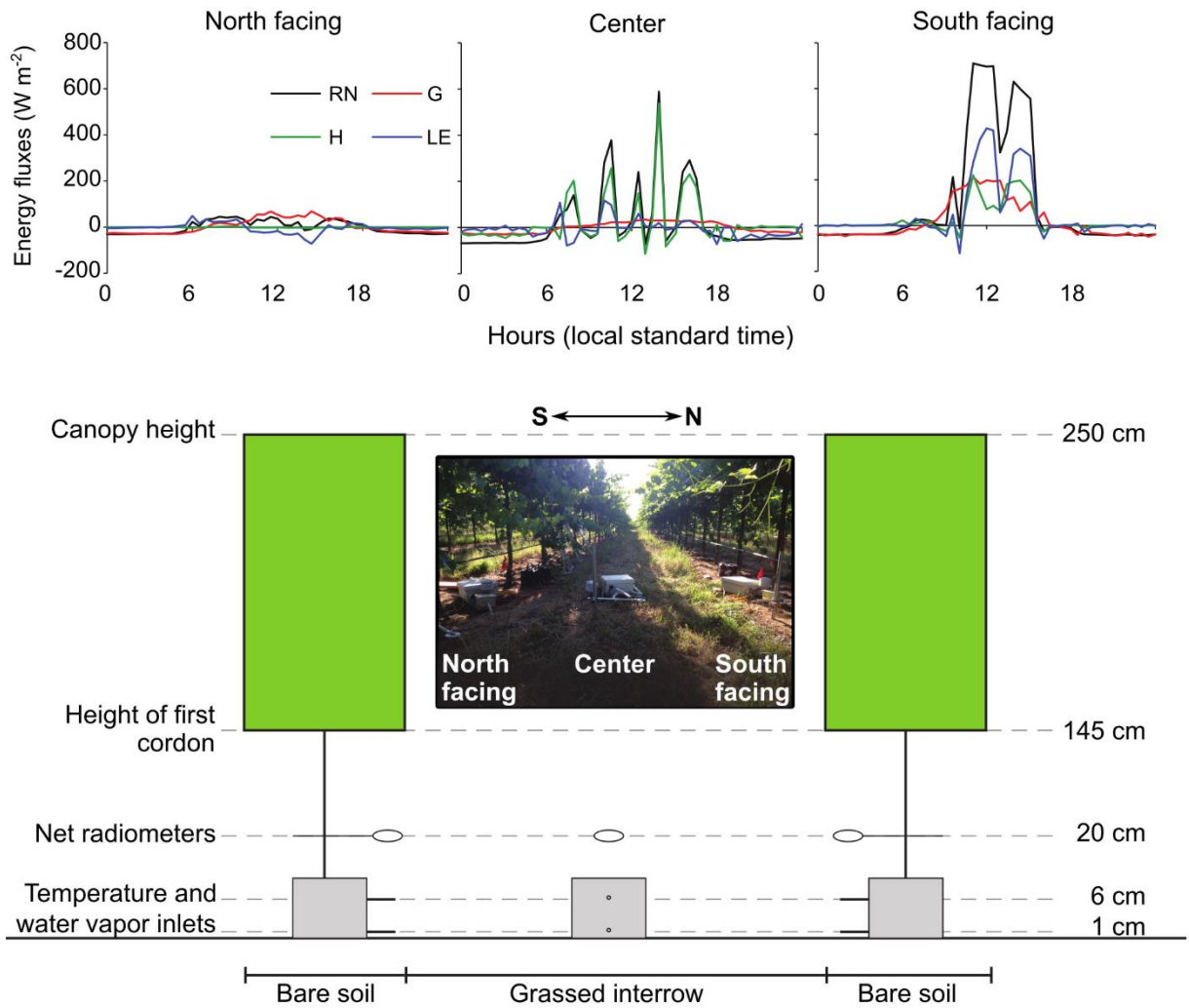
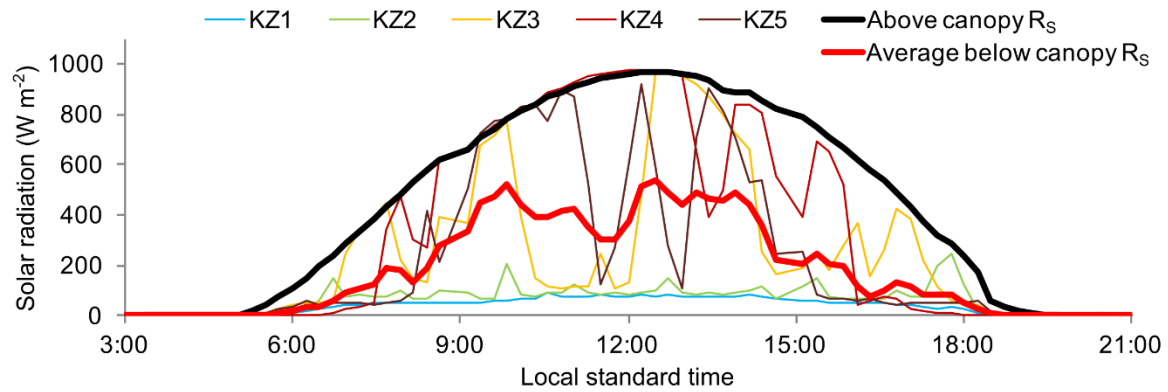


Figure 9. The surface energy balance components (top) for a day during IOP2 in June, 2015 as measured by micro-BR systems located under the vines in bare soil area for the north facing vine row (the vine row south of the center of the interrow), for the interrow and for a south facing vine row (the vine row north of the center of the interrow). Additionally a schematic with photo (bottom) illustrating the micro-BR deployment and measurement design.

**a. North vineyard 2015 IOP 3 using Kipp&Zonen (KZ)**



**b. South vineyard 2015 IOP 3 using Apogee (AP) and Epply (PSP)**

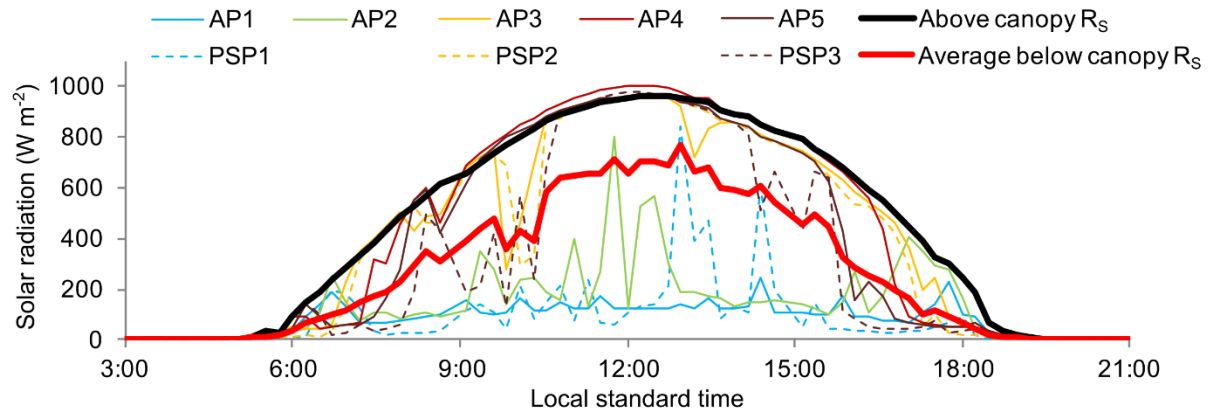


Figure 10. Diurnal radiation measurements above and below the vine canopy using 5 to 8 radiation sensors at north (site 1) and south (site 2) vineyard, respectively, for a clear day during IOP 3 (July 11) in 2015.

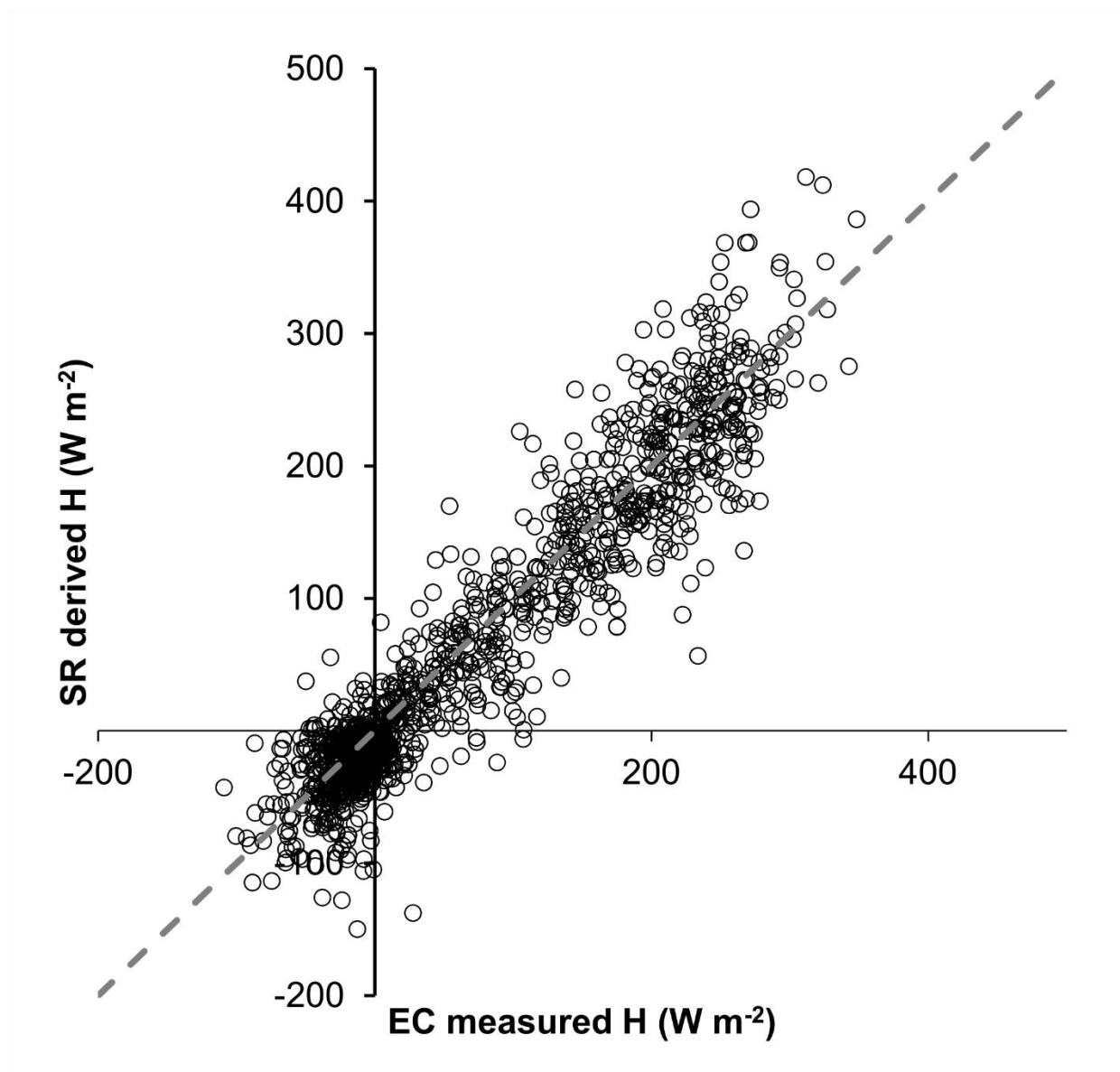


Figure 11. Hourly sensible heat flux (H) from eddy covariance measured at the south (site 2) vineyard flux tower, and hourly H from the stand-alone surface renewal for the 2015 growing season. Dashed line indicates perfect agreement (1:1 line).

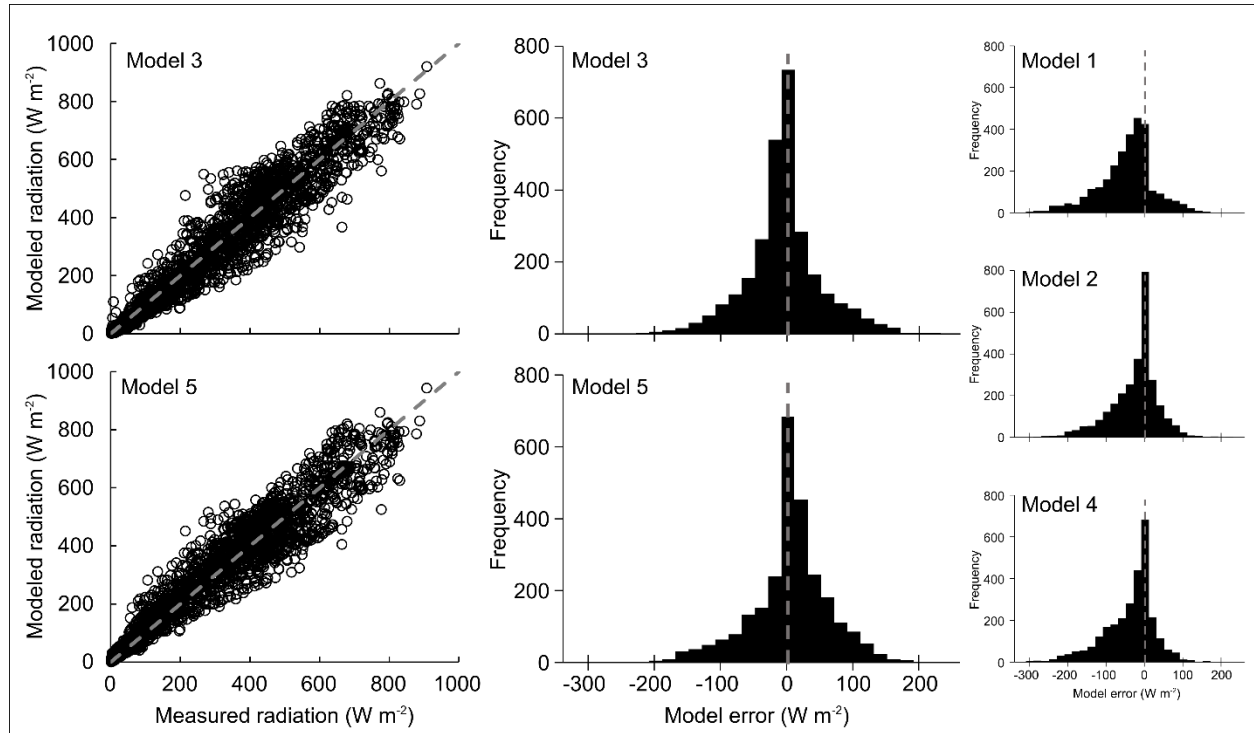


Figure 12. Comparison of solar radiation divergence model estimates with different levels of complexity (models 1-5) versus the below vine canopy solar radiation measurements (15 min averages). Error histograms for all the models indicate the least bias and smallest error with the observations are from using models 3 and 5. Scatter plots for models 3 and 5 are provided with dashed grey line indicating perfect agreement with observations (1:1 line)..

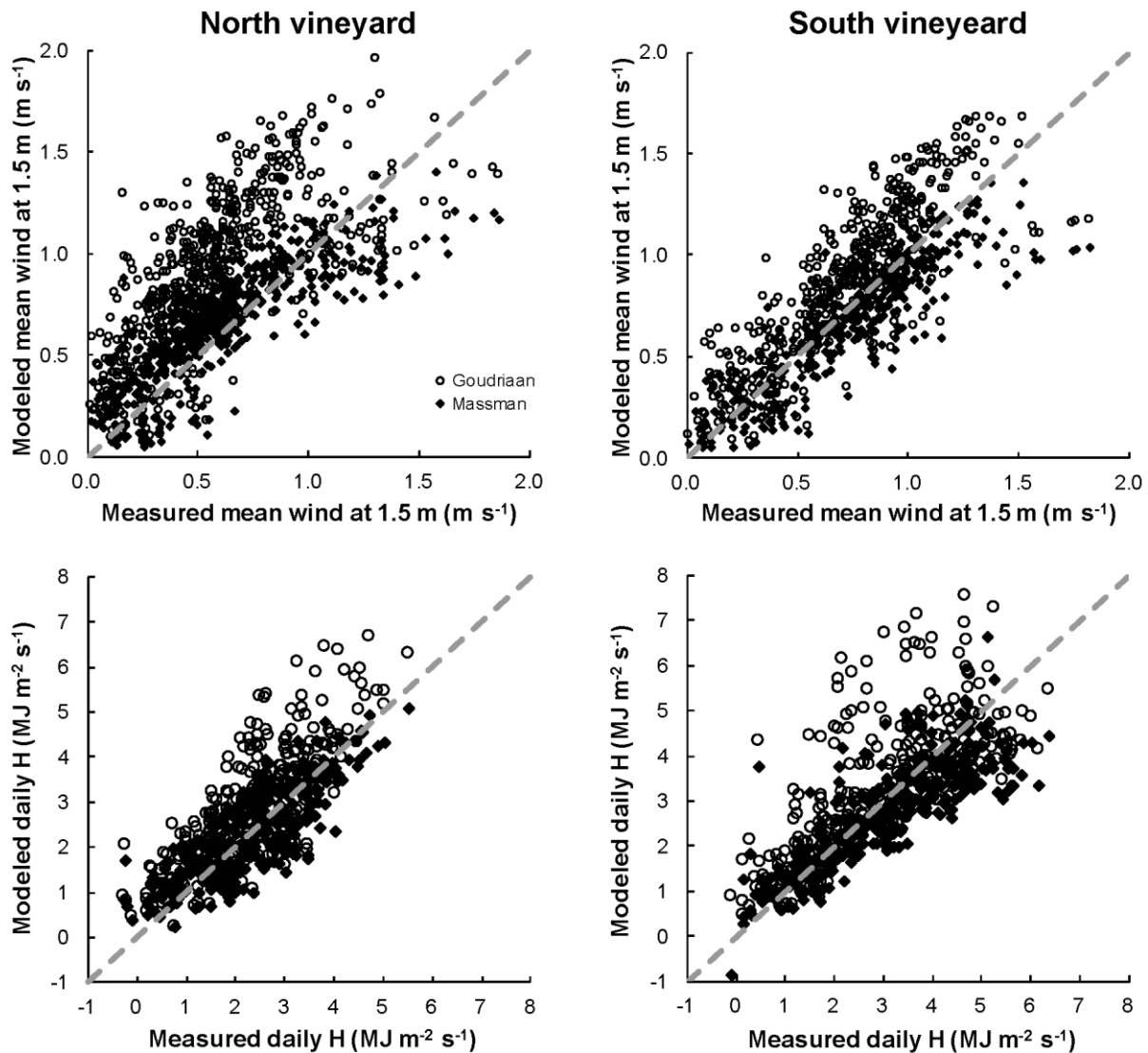


Figure 13. Comparison of (top) measured 1.5 m wind speeds versus TSEB values (15 min averages) derived using the Goudriaan and Massman within-canopy wind extinction formulations for the north and south vineyards (sites 1 and 2), and (bottom) resulting impact on daytime-integrated sensible heat flux estimates over the 2015 growing season. Dashed line represents perfect agreement with the observations (1:1 line).



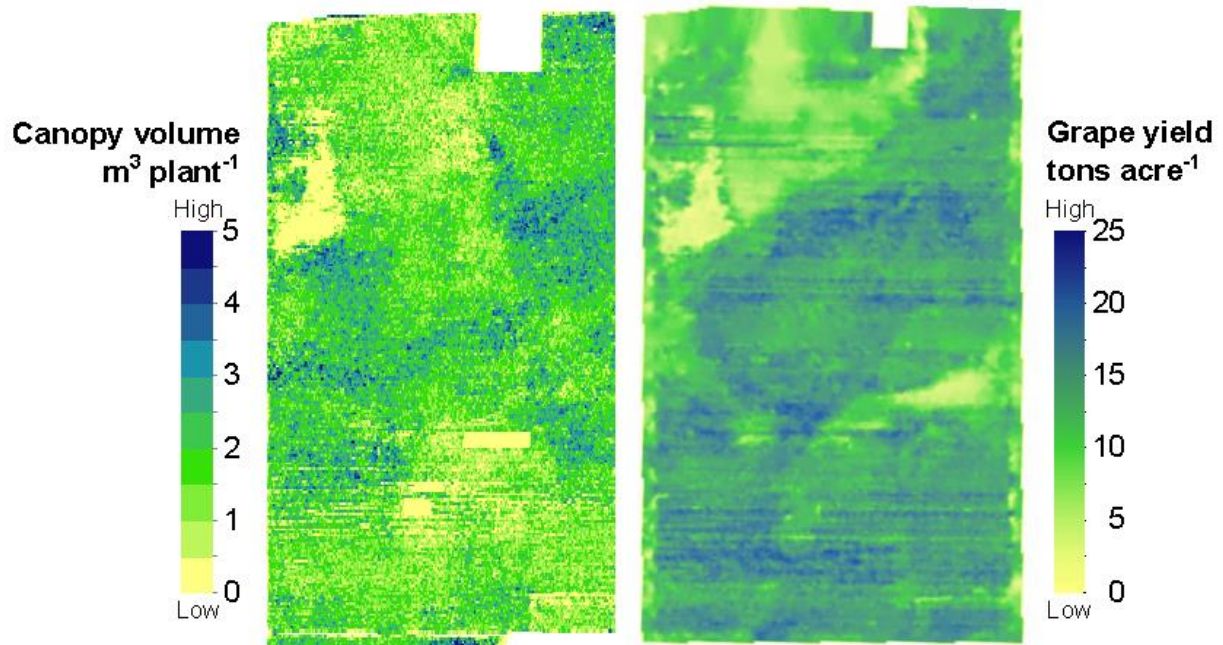


Figure 14. Example of canopy volume estimated for individual vines for an AggieAir UAV flight in August 2014 and the 2014 yield map the north vineyard. Note the variability in canopy volume across the field and an area of highly stressed or dead vines in the upper left with little or no biomass.

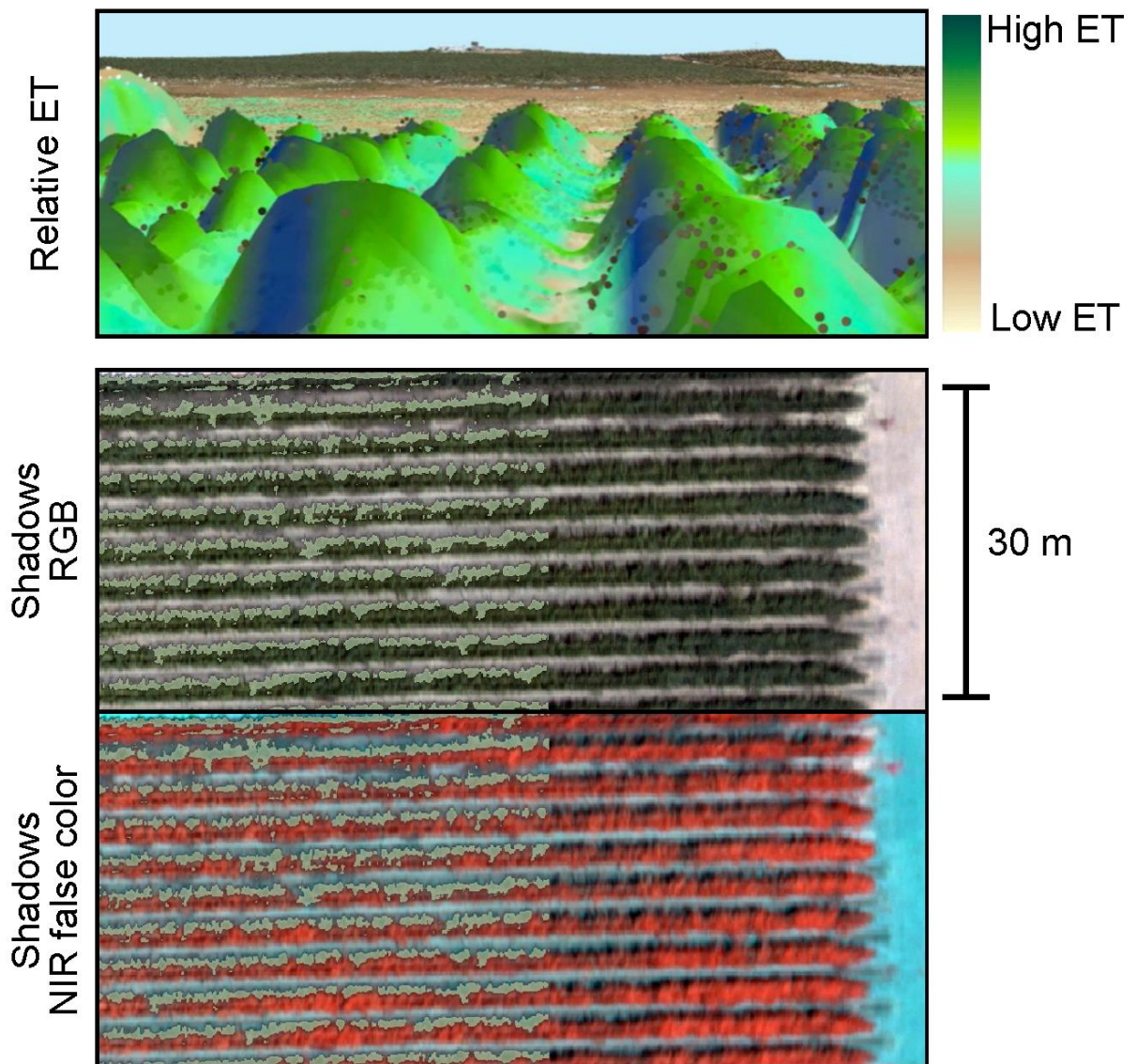


Figure 15. (Top) Variation in modeled ET due to shadow/micro-topography effects, generated using a DSM for a vine row viewed at different angles. Black/grey dots are the point cloud data. (Bottom) Automated identification of shadow locations (light green color) along several rows overlay red-blue-green (RGB) and near-infrared (NIR) false color UAV imagery.

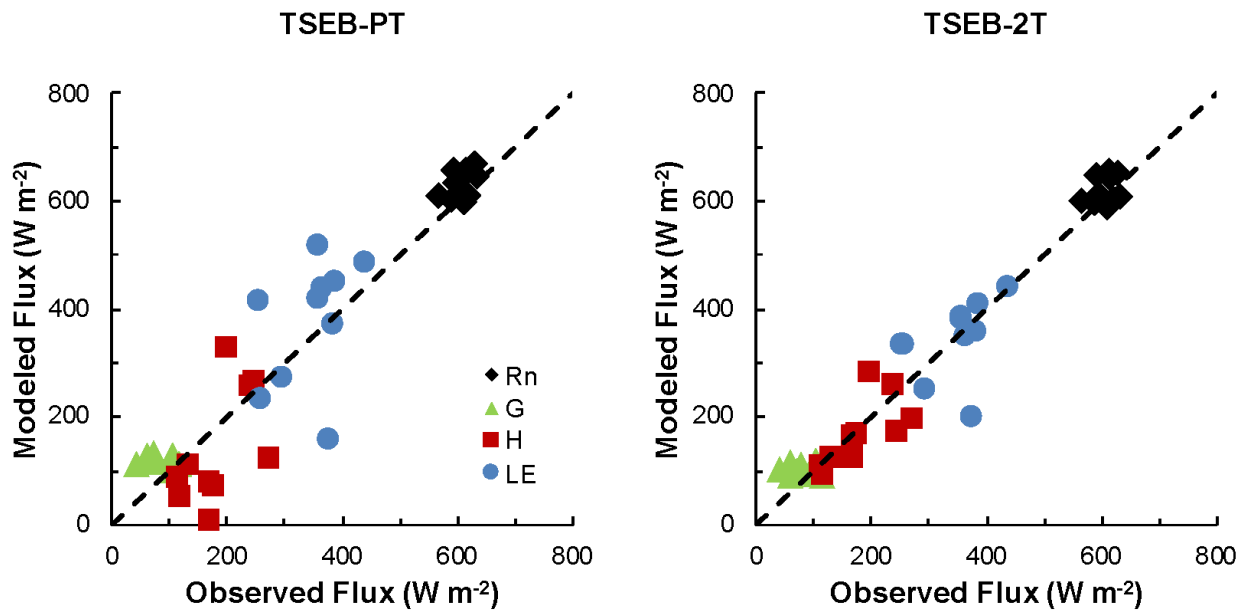


Figure 16. Comparison of TSEB flux estimates with energy balance components (net radiation (RN), soil heat (G), sensible heat (H) and latent heat (LE)) measured at the time of UAV overpass during flights in 2014 and 2015. Model results are shown (left) using composite temperatures and TSEB-PT, and (right) using component temperatures and TSEB-2T. In both cases, the TSEB models were modified to account for radiation and wind transmission through row crops.



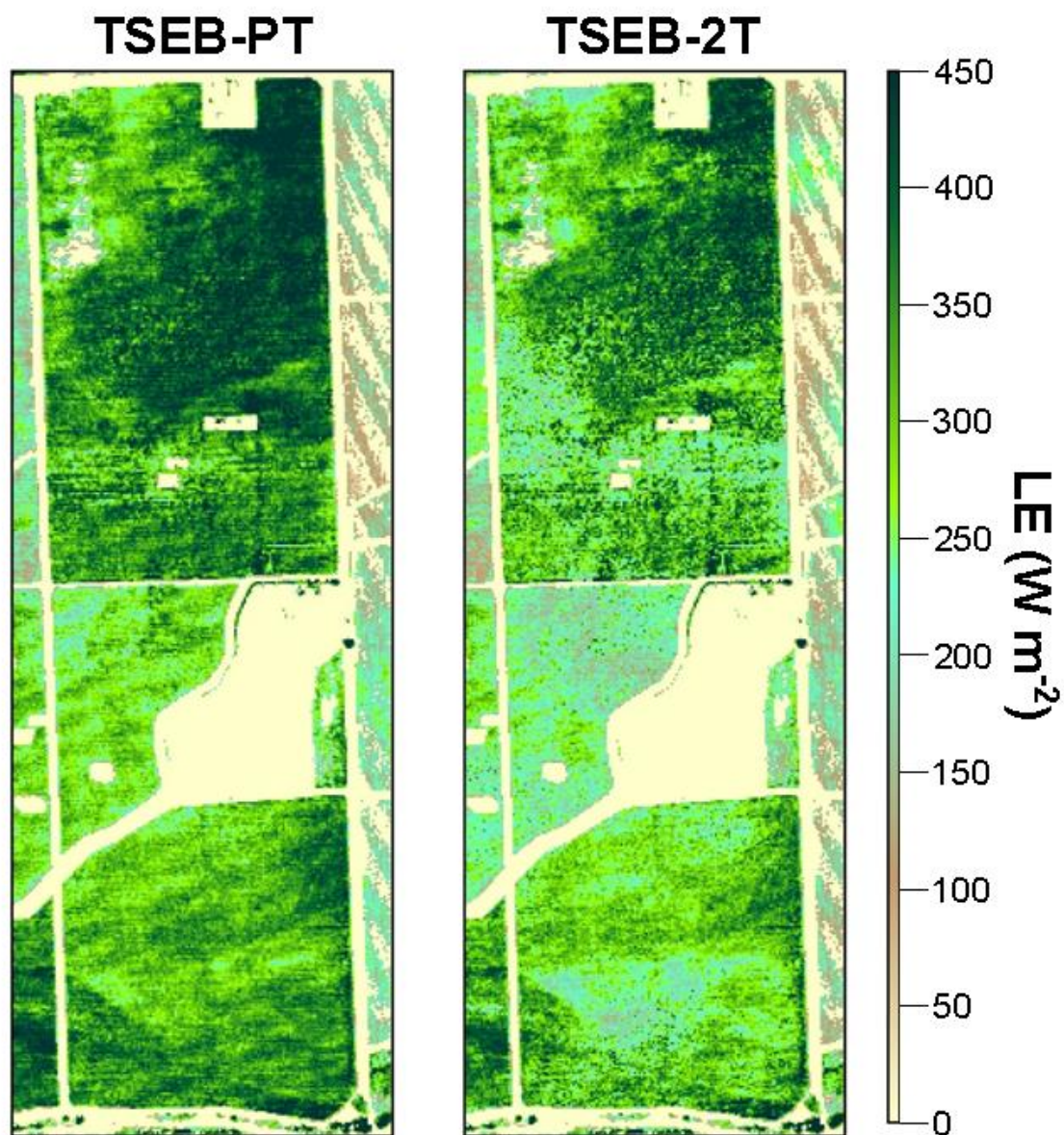


Figure 17. Latent heat fluxes (LE) maps at 3.5 m resolution computed using TSEB-PT and TSEB-2T from the UAV imagery collected at the time of Landsat overpass on August 9, 2014.

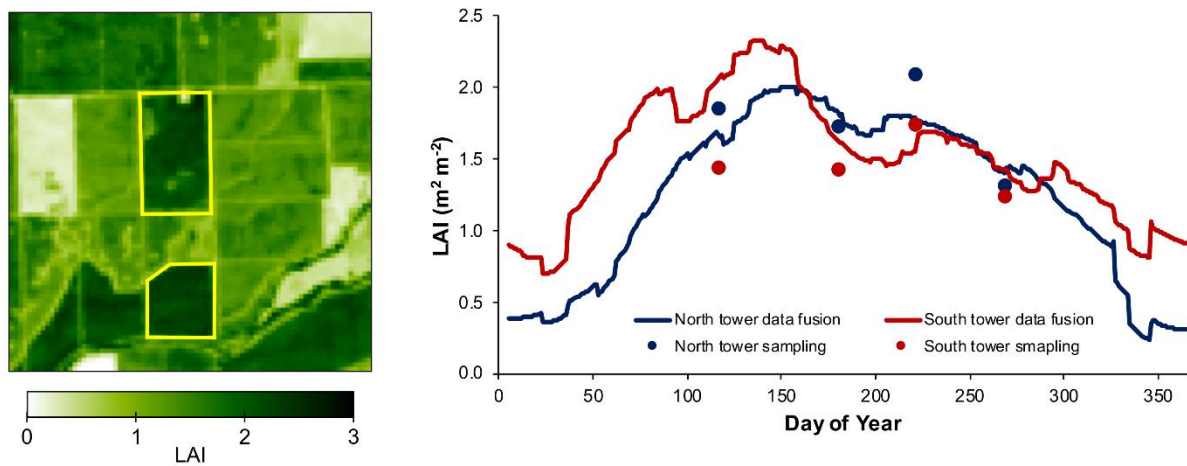


Figure 18. On the left is a map of LAI at 30 m resolution for north and south vineyards within the yellow boundaries at around peak LAI for year 2014 growing season while on the right a comparison of ground measured versus satellite derived daily LAI near the flux towers in north and south vineyards over the 2014 growing season (see Sun et al., 2017 for details).

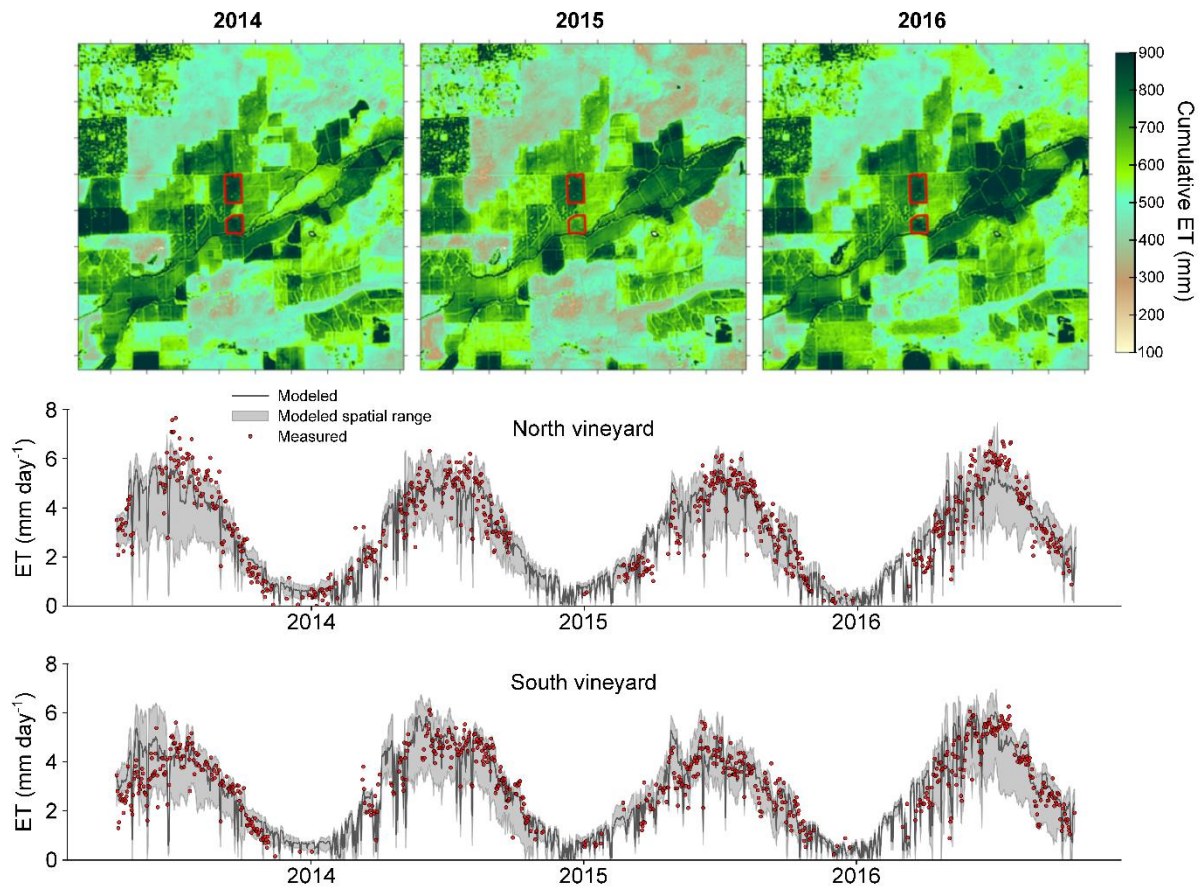


Figure 19. Cumulative ET (mm) map at 30 m resolution over the growing season (March 1-September 1) for a 9 x 9 km area surrounding the north and south GRAPEX vineyards (top) and daily ET modeled over the estimated tower footprint (black line) as well as the maximum and minimum (range) in ET versus observed (red dots) for the north (site 1) and south (site 2) vineyards (bottom).



## 2017 GRAPEX Sites

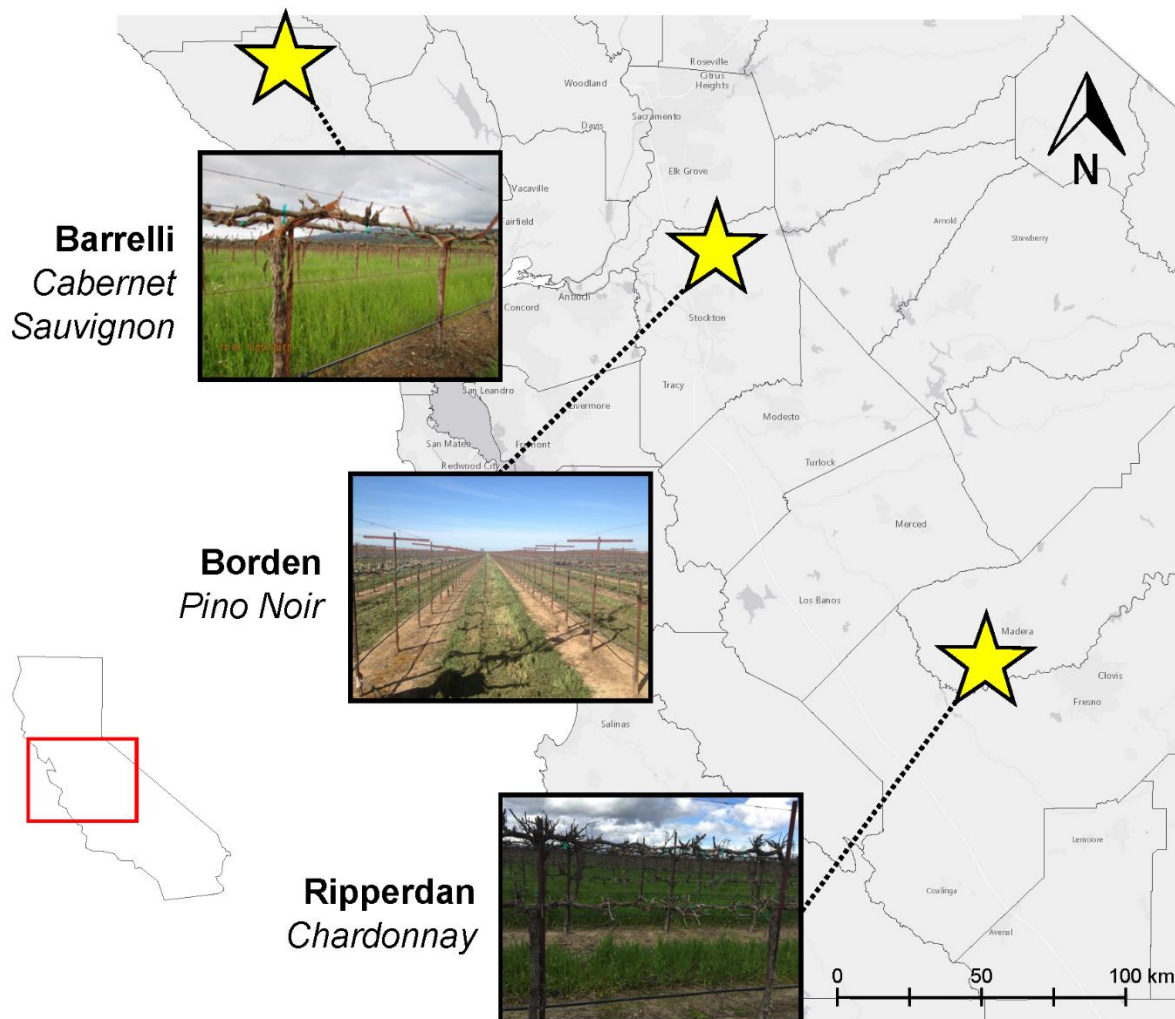


Figure 20. The expansion of 2017 GRAPEX experimental vineyard sites from Borden site to Barrelli vineyard to the north and Ripperdan vineyard to the south spanning a large range in degree day accumulations (see text) and vine varieties and trellis designs.